Simulation and Optimization of Friction Stir Process of Aluminum 7075-T6 Alloy

Vahid Gharibvand

Submitted to the
Institute of Graduate Studies and Research
in partial fulfillment of the requirements for the degree of

Master of Science
in
Mechanical Engineering

Eastern Mediterranean University
February 2021
Gazimağusa, North Cyprus

Approval of the Institute of Graduate Studies and Research

Prof. Dr. Ali Hakan Ulusoy
Director

I certify that this thesis satisfies all the requirements as a thesis for the degree of Master of Science in Mechanical Engineering.

Prof. Dr. Hasan Hacisevki
Chair, Department of Mechanical Engineering

We certify that we have read this thesis and that in our opinion it is fully adequate in scope and quality as a thesis for the degree of Master of Science in Mechanical Engineering.

Asst. Prof. Dr. Babak Safaei
Supervisor

Examining Committee

1. Assoc. Prof. Dr. Shaban Ismael Albrka

2. Asst. Prof. Dr. Mohammad Bsher A. Asmael

3. Asst. Prof. Dr. Babak Safaei

ABSTRACT

In recent decades, friction stir process (FSP) has become a popular manufacturing method for joining metals especially in automotive and aerospace industries. Aluminum alloys match the requirements of aircraft and automobile production due to the balance between light weight and strength as well as resistance to rust and corrosion. In the present study, Abaqus®/Explicit CAE 2017 (Complete Abaqus® Environment) with built-in Johnson-Cook material flow algorithm was used to model the friction stir process for joining two AA7075-T6 Aluminum alloy plates under different rotation and linear speeds. The trade-off analysis can be performed in three-dimensional numeric domain before joining the alloys in experiments. This study used Eulerian finite-element simulation for the workpiece and Lagrangian simulation for the tool. The present study simulated tool rotation speed at 135, 500, 1000, 1500, 2000, 2500 rpm. Also, traverse speed was simulated at 16, 25, 50, 75, 100, 125 mm/min. The effects of different parameters on the temperature, material flow, and microstructures in SZ and TMAZ zones were evaluated. Taguchi DOE determined the optimum FSP/FSW process parameters at 1500 rpm rotation, 50 mm/min traverse, and 20 rev/mm pitch to generate the highest tensile strength. This study demonstrated that Abaqus®/Explicit is a powerful tool for engineers and researchers to develop optimized 3D numeric models. The Abaqus® inputs can be modified to adjust FSP parameters and simulate the thermo-mechanical goals that must be achieved in industrial applications. Optimum non-linear 3D model will minimize lab experimentation and will result in significant industrial cost savings. The findings of present study are useful for industrial manufacturing, future scientific studies of alloy compositions, and finding new alloys optimized for emerging industrial applications.

Keywords: Friction stir processing, Microstructures, Thermo-mechanical properties, Eulerian simulation, AA 7075-T6, Taguchi optimization.

ÖZ

Son yıllarda, sürtünmeli karıştırma işlemi (FSP), özellikle otomotiv ve havacılık endüstrilerinde metalleri birleştirmek için popüler bir üretim yöntemi haline geldi. Alüminyum alaşımları, hafiflik ve mukavemet arasındaki dengenin yanı sıra pas ve korozyona karşı direnç nedeniyle uçak ve otomobil üretiminin gereksinimlerini karşılar. Bu çalışmada, iki AA7075-T6 Alüminyum alaşımlı plakayı farklı dönüş ve doğrusal hızlarda birleştirmek için sürtünmeli karıştırma işlemini modellemek için yerleşik Johnson-Cook malzeme akış algoritmasına sahip Abaqus® / Explicit CAE 2017 (Tam Abaqus® Ortamı) kullanılmıştır. Takas analizi, alaşımları deneylerde birleştirmeden önce üç boyutlu sayısal alanda gerçekleştirilebilir. Bu çalışmada, iş parçası için Euler sonlu eleman simülasyonu ve takım için Lagrange simülasyonu kullanılmıştır. Mevcut çalışma, 135, 500, 1000, 1500, 2000, 2500 rpm'de takım dönüş hızını simüle etti. Ayrıca travers hızı 16, 25, 50, 75, 100, 125 mm / dak olarak simüle edildi. Farklı parametrelerin SZ ve TMAZ bölgelerinde sıcaklık, malzeme akışı ve mikroyapılar üzerindeki etkileri değerlendirildi. Taguchi DOE, en yüksek gerilme mukavemetini oluşturmak için 1500 rpm dönüş, 50 mm / dak travers ve 20 rev / mm aralıkta optimum FSP / FSW işlem parametrelerini belirledi. Bu çalışma, Abaqus® / Explicit'in, mühendisler ve araştırmacılar için optimize edilmiş 3B sayısal modeller geliştirmek için güçlü bir araç olduğunu gösterdi. Abaqus® girişleri, FSP parametrelerini ayarlamak ve endüstriyel uygulamalarda ulaşılması gereken termo-mekanik hedefleri simüle etmek için değiştirilebilir. Optimum doğrusal olmayan 3B model, laboratuvar deneylerini en aza indirecek ve önemli endüstriyel maliyet tasarrufu sağlayacaktır. Bu çalışmanın bulguları, endüstriyel üretim, alaşım bileşimlerinin gelecekteki bilimsel çalışmaları ve ortaya çıkan endüstriyel

uygulamalar için optimize edilmiş yeni alaşımların bulunması için faydalıdır.

Anahtar Kelimeler: Sürtünme karıştırma işlemi, Mikro yapılar, Termo-mekanik özellikler, Euler simülasyonu, AA 7075-T6, Taguchi optimizasyonu.

TO MERCIFUL GOD AND TO MY FAMILY

ACKNOWLEDGMENT

First and foremost, I am thankful to God for granting me the strength to carry on my studies and research activities especially in the difficult era of COVID-19 pandemic.

I benefited immensely from the wise guidance and great support extended by several intelligent people who inspired me to finish this work. I must express my deep appreciation to my thesis supervisor, Assistant Professor Dr. Babak Safaei, for his strong guidance, constant encouragement, great attention to detail and for helping to keep me on schedule. In addition, I have a big debt of gratitude to Assistant Professor Dr. Mohammad Asmael for providing great support during my academic studies and for offering profound advice and wise suggestions during my thesis research project.

I am very grateful to my dear parents, sisters, and brothers for selflessly offering moral support, financial assistance, and emotional backing under all circumstances. Also, I must sincerely thank all my friends who provided good encouragement and increased my self-confidence during the current global pandemic.

PREFACE

The first passion in my life since childhood has always been to figure out how various materials and physical objects behave and interact with each other. For this reason, I decided to study mechanical engineering in both undergraduate and graduate programs. After successful defense of this master's degree thesis at EMU, my next goal is to continue mechanical engineering studies to earn a PhD degree in the future. My second passion has been learning about advanced computational technologies and computer simulation tools that can be helpful in the field of mechanical engineering. I believe the best way to accelerate new innovations in my beloved field of mechanical engineering is to leverage the recent advances in computer hardware and software and push for industrial automation. This is the reason I decided to use the Abaqus®/Explicit tool for computer simulation of my master's degree research thesis on friction stir process of AA 7075-T6 alloy.

TABLE OF CONTENTS

LIST OF TABLES

LIST OF FIGURES

LIST OF SYMBOLS AND ABBREVIATIONS

°C	Degrees Centigrade
µm	Micron
2D	Two Dimensional
3D	Three Dimensional
4D	Four Dimensional
AA	Aluminum Alloy
ALE	Arbitrary Lagrangian-Eulerian
AS	Advancing Side
BM	Base Metal
CAGR	Compound Annual Growth Rate
CEL	Coupled Eulerian-Lagrangian
Cr	Chrome
Cu	Copper
CW	Clockwise
DOE	Design of Experiment
Fe	Iron
FEM	Finite Element Model
FSP	Friction Stir Processing
FSW	Friction Stir Welding
Gpa	Giga Pascal
HAZ	Heat-Affected Zone
HV	Hardness Vickers
Ksi	Kilopound Per Square Inch

MGS	Mean Grain Size
Mpa	Mega Pascal
mm/min	Millimeter Per Minute
R&D	Research and Development
RPM	Revolutions Per Minute
RS	Retreating Side
SSW	Solid State Welding
SZ	Stir Zone
TEM	Transmission Electron Microscopy
TiC	Titanium Carbide
TMAZ	Thermo-Mechanical-Affected Zone
TS	Tensile Strength
USD	United States Dollar

Chapter 1

INTRODUCTION

1.1 Aluminum History and Current Status

Early history of Aluminum compounds goes back thousands of years. For example, Egyptians used Alum (aluminum potassium sulfate KAl (SO4)2) more than 5,000 years ago for application as dye fixer. Persians used clays containing aluminum silicates to make pots with more strength over 5000 years ago. Also, ancient Greeks used anhydrous aluminum sulfate (Al2(SO4)3) to stop bleeding from minor wounds which was the precursor to modern styptic pencils used today. Some European chemists conducted a lot of experimentation in the 18^{th} century to produce aluminum metal. The discovery of Aluminum metal finally took place in nineteenth century. An American researcher Charles Martin Hall and a French researcher Paul Louis-Toussaint Héroult made simultaneous discovery of aluminum metal in 1886. The discovery was named after both researchers as Hall-Héroult process which is still in use today. Charles Martin Hall and some investors founded a new company called Aluminum Company of America in 1907. The company is now operating under the name Alcoa and is the biggest aluminum producer in the world [1].

1.1.1 Global Aluminum Production

There are two upstream operations for production of Aluminum which consist of bauxite mining and alumina refining. The main ore of Alumina is a residual rock called bauxite (Al_2O_3). A vast majority of worldwide bauxite resources are in the countries located near tropical regions of earth such as central and south America, Africa,

Australia, Vietnam, and India. Each year, more than 160 million metric tons of bauxite are mined and shipped to alumina refineries around the world. Alumina refineries in turn ship their output to smelters which further process the material by using Hall-Héroult method to produce aluminum metal [2].

1.1.2 Aluminum Alloys

Pure Aluminum which is not alloyed with other materials is soft and does not have much strength. As a result, it is not suitable for most applications. Therefore, Aluminum is alloyed with other non-metal and metal elements such as zinc, iron, magnesium, manganese, silicon, etc. in varying quantities. The alloyed metals have improved mechanical properties and strength which enables them to be useful in a wide variety of transportation, structural, and other applications. There are more than 540 registered Aluminum alloy compositions available today [3].

1.1.3 Aluminum Usage in Modern Applications

The pure Aluminum (Al) metal is soft and light weight with silver gray color. The pure Aluminum metal is not suitable for structural applications due to lack of strength. However, the mechanical and physical properties of Aluminum can be modified significantly by adding other alloy elements such as manganese, copper, magnesium, zinc, etc. As a result, the right Aluminum alloy properties can be optimized to fit a wide variety of industrial applications. In addition, Aluminum can be recycled again and again because its properties do not degrade with reprocessing and recycling. Aluminum and recycled Aluminum are used today to produce cars, airplanes, boats, bicycles, houseware, cans, etc. [4]. In 2018, worldwide Aluminum market size for car and vehicle production was estimated to be USD 33.76 billion. Worldwide automotive Aluminum usage in car production is expected to grow by compound annual growth rate (CAGR) of 8.7% from 2019 to

2025. There is growing market demand for new automobiles in North America, Europe, and Asia Pacific regions. The demand for new vehicles is especially growing in large countries like United States, China, and Germany which means the demand for components made with Aluminum components will be higher year after year in the foreseeable future. Figure 1.1 shows the use of Aluminum in production of various types of automobiles in the world [5].

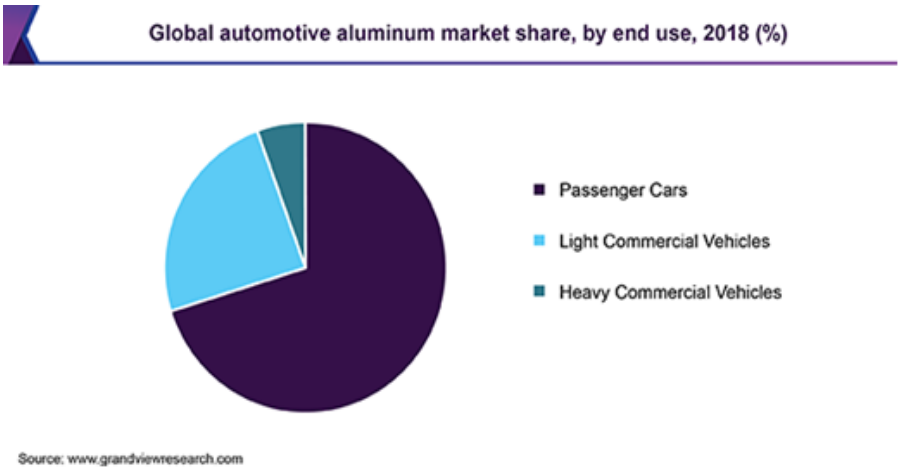

Figure 1.1: Global automotive aluminum usage, 2018 [5]

Aluminum usage is growing in manufacturing various car components such as vehicle roof, doorframes, new hybrid engines, etc. For example, it was reported that Mercedes Benz GLA and Mercedes Benz S Class (W222) had around 240 kg and 380 kg of aluminum content as of 2016, respectively [5]. In 2013, Ford's President and CEO Mr. Alan Mulally granted some interviews to the press in connection with the announcement of the then new F-150 truck and praised the widespread use of Aluminum by Ford. Mr. Mulally said; "pound for pound, aluminum is stronger and tougher than steel, and aluminum will be the material of choice for Ford moving forward" [6]. Figure 1.2 shows the usage of Aluminum in production of various types of automobile structures in the U.S. [7].

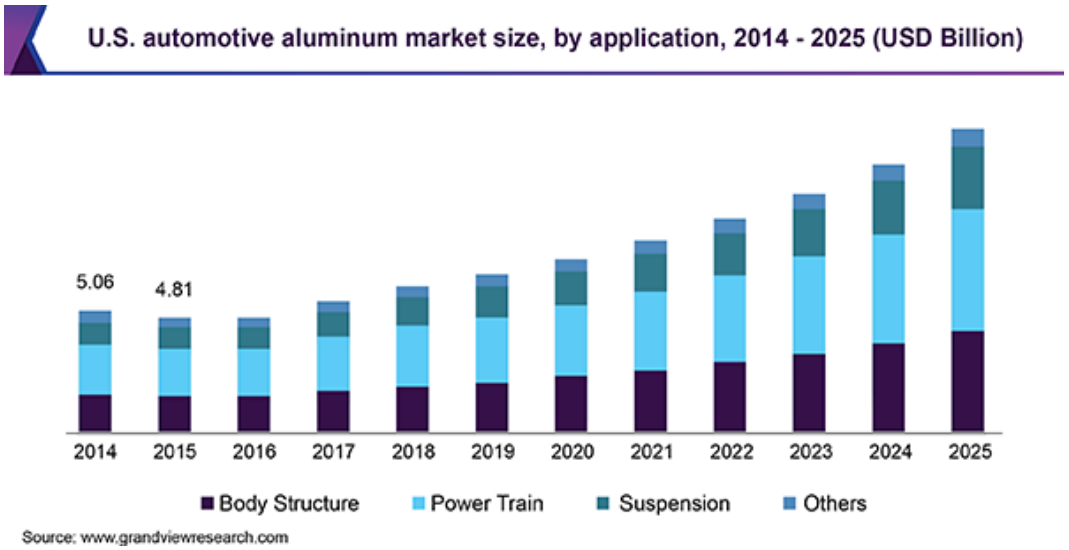

Figure 1.2: U.S. aluminum usage by automotive application [7]

Another large market for Aluminum high-strength alloys is the aerospace sector. The worldwide market size for high-strength Aluminum alloys was estimated to be USD 31.15 billion in 2019. High-strength sector is expected to increase at compound annual growth rate (CAGR) of 3.5% from 2020 to 2027. The aerospace industry is a large user of high-strength Aluminum in the world and will account for large growth in this market. High-strength Aluminum alloys offer unique advantages to aircraft design engineers as they strive to build the next-generation of aerospace systems. The worldwide high-strength markets and especially aircraft manufacturer like Boeing and Airbus have experienced severe negative impact in 2020 from the unfortunate global outbreak of the COVID-19 virus. It is expected that the negative impact on aircraft manufacturing and many other aerospace applications will likely continue for some time into 2021 and beyond. In addition to aerospace sector, all other manufacturing industries that use various compositions of high-strength Aluminum alloys have experienced significant negative downturn with disruption in their production and supply chains as a result of the global spread of the COVID-19 pandemic. Figure 1.3

shows the U.S. high-strength Aluminum usage in aerospace, automotive, railway & marine, defense & space, and other categories [8].

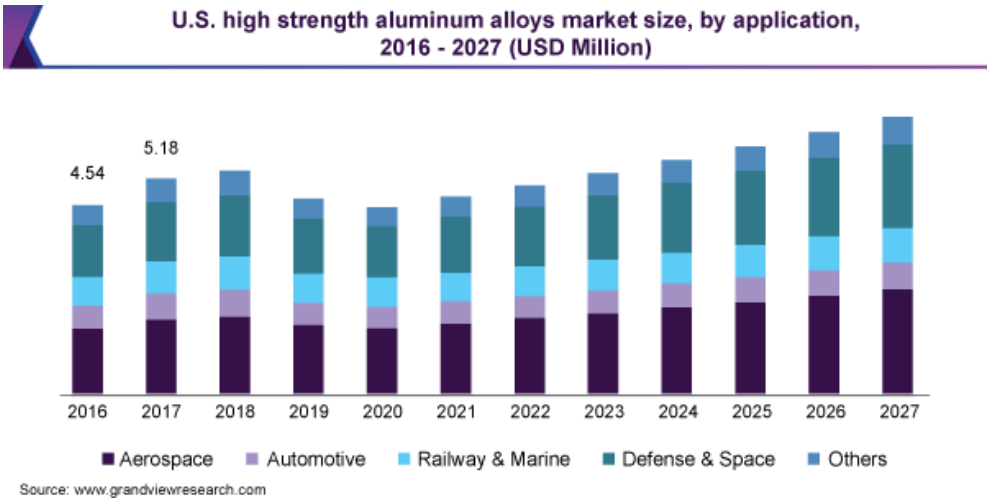

Figure 1.3: U.S. high-strength aluminum usage by application [6]

1.1.4 Aluminum AA7075-T6 Alloy

The present research study is focused on finite-element 3D numerical simulation of FSP process for joining two identical Aluminum alloys (AA) of AA7075-T6. This alloy contains zinc as the primary alloying element which results in high strength comparable to steel despite the light weight of AA7075-T6. This alloy offers good fatigue strength but average machinability in industrial production. The biggest advantage of AA7075 alloy is its high strength-to-density ratio which is ideal in manufacturing various components for transportation applications such as aviation, automotive, and marine [9]. AA7075 has temper designations and definitions. The T6 designation is defined as solution heat-treated first and aged artificially later. T6 temper has a typical tensile strength (TS) of 83 kilopound per square inch (Ksi) which is even better than many forms of mild steel metal [10]. The most common form of Aluminum thermal treatment is called Solution Heat Treatment. This is a process developed to heat the alloy to high temperature around 990 Degrees Fahrenheit. The alloy is first placed in the solution. The

next step is quenching the alloy in water to make supersaturated solution around normal room temperature. After solution heat treatment is completed, the next process is called aging which allows the precipitation of a part of the elements from the supersaturated solution to achieve the desired mechanical properties in the alloy [9]. High-strength Aluminum alloy AA7075 (Al-Zn-Mg-Cu) can be hardened and used in demanding applications such as aerospace, defense, marine and automotive. The friction stir technique is a reliable method for joining AA7075-T6 alloys. The chemical composition of AA7075-T6 is presented in Table 1.1 [11]. The basic mechanical properties of AA7075-T6 alloy are presented in Table 1.2 [12].

Table 1.1: Chemical compositions of 7075-T6 aluminum alloy (wt.%) [11]

Element	Zn	Mg	Cu	Fe	Si	Ti	Mn	Cr	Al	Other
Wt.%	5.6	2.5	1.5	0.5	0.4	0.2	0.3	0.25	87.1–91.4	0.15

Table 1.2: Basic mechanical properties of AA7075-T6 aluminum alloy [12]

Density x1000 [kg/m3]	Elastic modulus [GPa]	Ultimate tensile strength [MPa]	Yield strength [MPa]	Elongation [%]
2.81	71	578	469	33

1.2 Definition of the Problem

AA7075-T6 alloy is used frequently in several industries to manufacture many components that have higher strength and lower weight compared to other alloys. There is an industrial need to develop accurate three-dimensional (3D) non-linear numeric simulation models to analyze the FSP process for joining two AA7075-T6 alloys. The trade-off analysis of thermo-mechanical properties must be performed in 3D numerical

domain before physically joining the alloys in a lab environment or during industrial production.

1.3 Need for Research (Motivation)

Friction stir process is a new manufacturing method which was introduced in recent decades. This process is uniquely capable of retaining the mechanical properties of alloys during the joining process. FSP is flexible and efficient and therefore is superior to previous techniques. However, some aspects of FSP process must be better understood especially with respect to thermo-mechanical properties of new Aluminum alloys that are being developed by design engineers in different industries. Extensive friction stir research and development projects are undertaken around the world to increase the performance and reduce the production cost of new alloys. Several modified new alloy compositions with better properties have already been invented and the research to develop new alloys is continuing. The new compositions are optimized to match the exact thermo-mechanical requirements and production cost targets for specific system components that must be fabricated for advanced applications in industries such as transportation, aerospace, etc. It is very expensive to conduct advanced research and development (R&D) in any industry. In addition, there is high cost associated with purchasing Aluminum alloys for repeated experimentations in a lab or a factory. Therefore, it is faster and more cost-effective for design engineers to develop sophisticated 3D simulation models as the first step in materials research. This allows the engineers to perform trial-and-error evaluations of new alloys and develop a good understanding about the new alloy's behavior in terms of temperature distribution, grain size, stress, strain, plastic deformation, microstructure, etc. After the thermo-mechanical parameters are approximately optimized by using 3D numerical analysis technique, the design engineers can then

proceed to next step and conduct further experiments in laboratory by joining the new alloy to fine-tune the parameters needed for the desired industrial application.

1.4 Objectives of this Study

1. The main goal of the present research is to use the Eulerian finite element simulations of the workpiece to investigate the elastic-plastic thermo-mechanical behaviors in joining two identical AA7075-T6 Aluminum alloys using the friction stir process under different rotation and linear speeds. Although AA7075-T6 workpiece is modeled with Eulerian technique, the FSP tool is modeled with Lagrangian technique. A 3D thermal model will be developed using Abaqus®/Explicit CAE 2017 (Complete Abaqus® Environment).
2. The elastic–plastic–hardening isotropic Johnson–Cook model will be used to analyze the material flow behavior.
3. The mechanical properties of workpiece will be simulated and investigated for the FSP zone.
4. The effects of the FSP process on temperature will be simulated and analyzed in 3D numerical domain for different speed parameters.
5. The effects of different speeds and FSP parameters on material properties of the stir zone (SZ) and thermo-mechanical effected zone (TMAZ) will be simulated and analyzed.

Chapter 2

LITERATURE REVIEW

2.1 History and Evolution of Welding Techniques

Different welding techniques have existed throughout the history of mankind. For example, the first metal joining technique in human history was forge welding which was developed before 1000 BC. Another early example is electric arc welding which was first discovered in 1800 in United Kingdom. This technique conducts electricity through a piece of metal to create an electric arc to heat and weld the metal surface. Also, an American engineer discovered the first metal electrode arc welding technique in 1890 and applied for patent. Another example is oxygen-acetylene gas welding technique which was invented by French engineers in 1903 to use pure oxygen gas instead of ambient air. This technique boosted the flame temperature and enabled the localized melting of a workpiece. Throughout the period of 1900's, the existing welding methods were upgraded and many new technologies were developed including laser beam welding. An extraordinary progress was achieved in 1991 and thereafter with invention of new welding techniques that are in widespread use around the world today. The first significant progress in this period was the introduction of friction stir welding by TWI institute in 1991 [13].

The traditional methods for welding metals have been classified into fusion welding and solid-state welding. Fusion welding refers to any process that melts the materials that have similar compositions and melting points in order to join them together.

Basically, metals with similar properties can be combined chemically in their molten state although some surface treatments may be required prior to welding. This type of welding can be achieved by using consumable electrodes or proper filler materials. Some fusion processes require a neutral environment due to risk of metal oxidation. Fusion processes cause the creation of heat-affected zone (HAZ) in the metal because of high temperatures involved. Some examples of fusion process are tungsten inert gas (TIG), metal inert gas (MIG) and laser welding [14].

Solid-state welding (SSW) refers to any process that does not melt the metals to join them together. One of the advantages of this process is that solid-state welding does not involve metal oxidation. Some examples of SSW are friction welding, forge welding, and ultrasonic welding using ultrasonic acoustic vibrations. SSW technique produces a smaller number of microstructure defects such as pores and alloying elements because the metal is not heated to its melting temperature. Another advantage of SSW is relatively small HAZ area which tends to reduce the risk to the material's mechanical strength. Other advantages include similarity of mechanical properties between the weld area and bonded metals, ability to weld different alloy compositions, and lack of consumable materials. On the other hand, a disadvantage of SSW is the requirement for full surface cleaning and degreasing before welding is commenced [15].

2.1.1 New Welding Technologies and Trends

The future is bright for continued improvement of current welding techniques and development of new technologies. There is a trend to use modern technology for continuous refinement of welding parameters and tools. In addition, it is expected that industrial welding operations will be fully integrated with the rest of factory operations using agile manufacturing tools and production control methods. Also, welding process

will continue to be automated as the welding operations use computer information systems on the factory floor and are better integrated with other operations such as product design, development, and manufacturing.

An important new direction is the design of new composite materials that are designed specifically to enable better welding during the manufacturing processes of new products in different industries. The concept of design for weldability will become a key mechanical engineering requirement for research engineers around the world. Also, the trend will be accelerated for discovery of new alloy compositions with superior properties and higher strength. Some new smart materials will be developed with embedded semiconductor computer chips to monitor the reliability of the weldment throughout the product lifecycle to anticipate problems and send warning to initiate repairs before the joint fails. The welding industry around the world will have a tremendous range of opportunities to create multi-disciplinary innovations in development of new material compositions, advanced joining techniques, revolutionary hardware and software tools, sophisticated welding process modeling with 3D algorithms and transition to 4D domain.

The increasing pace of industrial automation will benefit welding development and integration across the full production life cycle. Finally, the development of smart materials and revolutionary techniques will enable significant reductions in energy requirements and production costs [13].

2.1.2 Overview of Friction Stir Welding (FSW) Technique

Friction stir welding (FSW) technique was the predecessor of the friction stir processing (FSP). The development of friction stir processing (FSP) technology was based on the evolution and refinement of the previous friction stir welding (FSW) technique. FSW

was invented in December 1991 by Wayne Thomas and his team of researchers at The Welding Institute (TWI) Ltd in United Kingdom. In the beginning, FSW was used to join thin-section Aluminum alloys for automotive and aerospace applications. The subsequent technology refinements have enabled FSW to successfully join other light metal alloys including titanium, as well as thick-section hard metals such as steel [16].

FSW applies mechanical energy to make the workpieces hot at a temperature below the melting point and then plastically deforms them. Unlike traditional methods, FSW technique does not use heat generator, electrode filler, and neutral environment. The basic operation of FSW technique involves the following steps. First, a shouldered rotating tool which is non-consumable and includes a profiled pin must be plunged into the workpiece metals. The metal faces that are intended to be joined must be abutting each other. Then, the continuous action of rotating tool causes frictional heat at the abutting interface which softens and joins the metals through linear motion in the direction of joint line [17]. FSW has turned into a significant joining technique especially for welding aluminum alloys used in making components for railways, ship-construction, and aerospace sectors. Globally, there are more than 135 licensees of the patented FSW technology with new applications and techniques being developed every day [18].

FSW process affects the microstructure of the materials being joined. There are four categories to classify the FSW microstructure of aluminum alloys: 1- unaffected zone, 2- heat affected zone (HAZ), 3- thermo-mechanically affected zone (TMAZ), stirred zone (SZ). These categories are defined based on heat effect and plastic deformation of the workpiece [19]. Major FSW parameters that can affect both the microstructure and the mechanical properties of the bonded joints include tool design and tilt angle, plunge

depth, axial force, welding and rotational speeds [20].

The evolution of microstructure during the FSW/FSP processing has been evaluated by several investigators. FSW technique is environmentally clean since metals are not melted and shield gas is not used. FSW can be used to join the 2xxx and 7xxx series of aluminum alloys which were difficult to weld with traditional welding techniques that existed before the invention of FSW. In addition, virtually any kind of alloy compositions of similar and dissimilar metals materials can be joined by using FSW process. The processes and operating principles for both FSP and FSW are similar. Both techniques would force the materials to undergo severe plastic deformation. Similarly, both FSW/FSP techniques can leverage friction heat and stirring to develop consistently refined microstructures [21].

2.1.3 Overview of Friction Stir Processing (FSP) Technique

Friction stir processing (FSP) technique has been derived from a previous-generation technique that was called friction stir welding. FSP was a state-of-the-art material-processing technology at the time it was put forward by Professor Dr. Rajiv Mishra in 1999 in connection with his research on superplastic materials [22].

FSP is a method for solid-state materials processing and therefore metal melting is not needed. As a result, crack defects and porosities associated with metal melting, cooling, and solidification do not occur. FSP offers several advantages compared to the conventional metal joining techniques. For example, many non-ferrous metals and alloys which contain very little iron and have low melting temperatures have been difficult to join with traditional welding methods in the past. However, FSP technique can join non-ferrous metals easily and reliably. In addition, FSP technique enhances the mechanical properties of the base metal and lowers the dilution rate of workpiece

materials. Only 20 years have now passed since the introduction of FSP in 1999. In this short period, FSP has expanded into new products and new markets. The work of Dr. Rajiv Mishra in United States to investigate optimum superplastic strain rates using friction stir processing has inspired similar new research around the world [23].

FSP was invented to make composite materials, to eliminate the casting defects locally, to refine the microstructures, and improve physical and mechanical properties such as creep, strength, fatigue, ductility, formability, and resistance to corrosion. However, there are important challenges such as tooling wear and new tool design that must be overcome to enable new applications in production of alloys that have high strength and high melting temperatures [24].

FSW/FSP processing of aluminum alloys has generated significant interest on the part of research engineers due to its potential to revolutionize the production processes in several important industries. It is critical to ensure the durability, safety, and structural integrity of components made with friction stir process. Therefore, it is important to evaluate the microstructural effects and material properties to optimize the FSP process parameters. There should be special emphasis placed on conducting detailed evaluation of FSP effects on the following important parameters: alloy superplasticity behavior, fatigue and tensile properties, hardness, microstructures, grain boundary, texture changes, recrystallization, and phase transformation [25]. FSP was initially intended to refine the Aluminum alloy microstructures and successfully develop superplastic materials. After the initial introduction, FSP gained widespread recognition as a new grain refinement technology to enhance the corrosion, tribological, and mechanical properties in several high-strength steel alloys as well as low-strength non-ferrous alloys. FSP parameters can be fine-tuned to fabricate a variety of micron to

nanostructured alloys. Many researchers around the world have experimented with different FSP process parameters and their findings have created new knowledge. The experimentations with tool rotation and travel speeds, additional cooling, and number of passes are providing valuable findings to assess the impact on material properties of new alloys. More recently, many experimentations with FSP tooling systems are conducted to improve the microstructures and mechanical properties of superalloys and hard alloys. FSP processing also offers the advantage of modifying or repairing the weld through microstructure modification [26].

2.2 Fundamentals of Friction Stir Processing

2.2.1 FSP Process Parameters

The steps involved in friction stir processing can be done with the same equipment used for friction stir welding. There is a tool that has a pin and shoulder. This tool is not consumable and it rotates to process the base metal. The rotation of the tool is in the counter clockwise direction. The axial force applies downward force on the shoulder. The direction of FSP is along the length of the workpiece alloy. After friction stir processing is initiated, the tool rotates quickly and plunges lower until its shoulder would make a contact with the surface of the workpiece alloy. Then, the tool will generate friction forces as it keeps rotating while passing through the workpiece in the direction specified for FSP. The friction contact between the tool shoulder and the alloy surface causes intense heat. The high temperature in turn would soften the base metal and cause significant plastic deformation in the FSP region around the steer zone (SZ). The plastic deformation causes some flow of the plastic alloy which remolds the workpiece material. The basic steps of FSP process are depicted in Figure 2.1 [27].

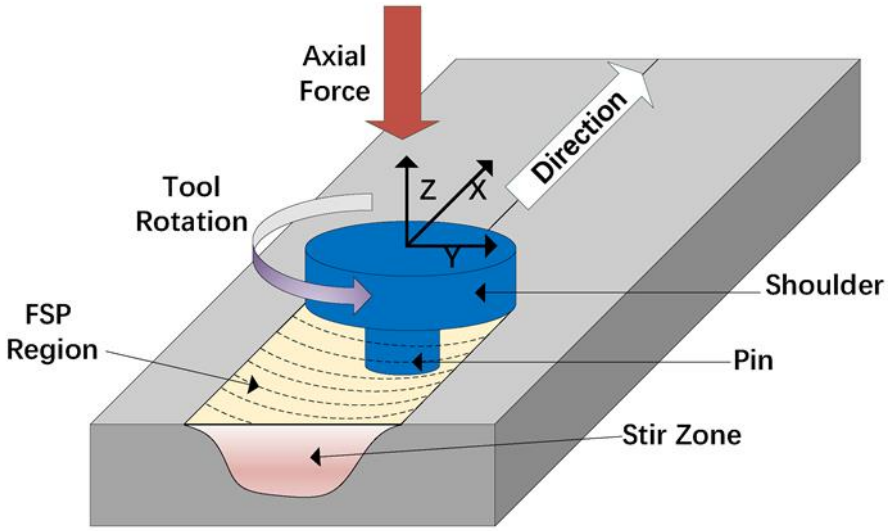

Figure 2.1: Friction stir process diagram [27]

Some researchers studied the vibration and frequency response of aluminum alloys with different FSW fatigue life properties. Their goal was to develop a better understanding about the correlation between the start of cracking from fatigue and the natural frequencies of each FSW type. These researchers investigated the process parameters for joining two Aluminum 7075-T6 alloys in a lap configuration using friction stir welding. The alloy used in this study had the following mechanical properties: density 2810 kg/m3, Young's modulus 71 GPa, and Poisson's ratio 0.33. The researchers used four different types of fatigue life in connection with joining two alloys under four different sets of friction process parameters. The lower sheet was placed on a supporting plate so that a rotating tool can press the top sheet. The rotating pin applied force in the downward direction and the pin's rotational speed softened the aluminum without melting the alloy. After the alloy was softened, the pin was able to penetrate into the metal. After the pin, the tool's shoulder made contact with the surface of the top sheet. The shoulder had larger surface compared to the pin. As a result, the shoulder was able to generate a higher level of heat and friction which then softened a larger region of the alloy. As the pin rotated, it pressed and stirred the two

alloys which created a metallurgical bond in the surrounding region of the pin. The tool was pulled back after frictions stir welding. The process created a typical distinct FSW hole in the middle of the workpiece weld. The researchers used experimental observations to study the growth of the fatigue cracks. Several fatigue tests of the alloys were performed in the laboratory as well as simulated using the Abaqus® software and Lancsoz method. Table 2.1 presents a summary with four sets of process parameters used by the researchers in the study [28].

Table 2.1: Summary of FSW process parameters [28]

	Shoulder Penetration [mm]	Rotating Toll Speed [rpm]	Vertical Pin Speed [mm/min]	Force Duration [ms]
Type 1	1.3	2500	8	5 to 6
Type 2	1.3	1600	8	5 to 6
Type 3	0.9	2000	8	5 to 6
Type 4	1.3	2000	8	5 to 6

In addition to making experimental fatigue tests, the researchers also developed 3D finite element (FE) numerical analysis to assess the relationship between the length of fatigue crack and the frequency response of fatigue modes. The FE mesh contained almost 34000 elements and maximum length of each was 3 mm. This study used 10-node quadratic tetrahedron for the type of mesh element. The findings of the FE simulation model were similar to the results of the experimental tests [28]. Figure 2.2 shows the FE mesh element for the lap FSP/FSW processing [28].

Figure 2.2: FE 10-node quadratic tetrahedron mesh [28]

The cast aluminum alloy contains defects and therefore has weak fatigue performance. Researchers used the friction stir processing to remove majority of the defects in a cast alloy and thereby strengthened its mechanical properties.

The researchers determined there was a link between the casting porosities and development of cracks in the alloy. After researchers removed the defects through FSP processing, they achieved five times improvement in fatigue life of Al–7Si–0.6 Mg cast alloy. Porosities caused a major increase in the growth rate of the cracks. The FSP process successfully removed the porosities and refined the Si particles which lowered the crack formation significantly. Also, the researchers found that the microstructural dimension affects the behaviors of the long crack and the short crack [29].

2.2.2 FSP Microstructure Modification

Microstructure modification is a result of FSP process caused by thermal-mechanical effects. The processing regions of FSP are normally classified as stir zone (SZ), thermo-mechanically affected zone (TMAZ), heat-affected zone (HAZ), and base metal zone (BM). FSP classification is similar to FSW [30]. The findings of a micro etching research study indicated that the microstructures in the SZ, BM, HAZ, and TMAZ zones were different. The micrographs indicated a major variation in grain size with 100 Micrometers (μm) in BM zone to 4-10 μm ultrafine grains in SZ zone [31].

The SZ region is made up from homogeneous refined equiaxed grains with sizes that decrease significantly compared to BM. During the FSP process, SZ is subjected to high temperature and undergoes major plastic deformation. This causes a transformation in its microstructure as a result of the dynamic recrystallization. Friction stir processing (FSP) was used to modify the microstructure and texture of an Mg-8Gd-5Y-1.1Nd-0.45Zr alloy. A solid solution (SS) alloy and an aging (AG) alloy were used and the results were compared. The findings showed that the size of grains in SZ zone were greatly reduced to 3–4 μm after FSP in both SS and AG alloys [32]. A friction stir processing (FSP) research study investigated the phase transformation and superelasticity in an alloy of TiNbTaZr. The researchers conducted multiple FSP passes. After recrystallization, existing dislocations were observed to gradually transition to sub-grain boundaries [33]. Another study investigated the effects of FSP processing on a Mg 6Zn 1Y 0.5Zr casting. FSP resulted in significant grain refinement and strong basal texture [34]. Another study focused on grain refinement during the microstructure evolution of Aluminum alloy AA6082-T6 alloy using bobbin FSW process. The research concluded that proportion of high-angle grain boundaries (HAGBs) in the FSP processing region increased after the completion of the process. In addition, the grain size experienced significant refinement and dropped from 100 μm in the base material (BM) to below 10 μm for the grains in stirring zone (SZ) [35]. FSP was processed on a Mg-Zn-Y-Zr alloy. FSP resulted in 4.5 μm ultrafine grains that had uniform distribution and had 91% high-angle grain boundaries which improved the plasticity in the BM zone [36].

Some researchers studied the influence of friction stir processing parameters on microstructure modifications in a cast NiAl bronze material using two methods of optical microscopy and transmission electron microscopy. A threaded type of pin was

used and different speeds were tested for tool rotation and traverse movement. The researchers observed serious stir zone deformation up to ~900 °C temperature. As tool rotation and traverse speed increased, almost total FSP microstructure modification was achieved around the peak temperature of ~1000 °C. In addition, the plastic material in the middle area of stir zone experienced very complex flow pattern caused by increasing speed. The pattern is known as onion ring structure. The research findings showed higher speed FSP processing generated higher peak temperature near the material surface that is in contact with the tool. Also, higher speed FSP processing created sharp temperature gradient relative to lower speed FSP processing [37]. FSP was used to process the Al–4Mg–1Zr microstructure with ultrafine grain size in the range of 0.7–1.6 μm. The deformation behavior was investigated at temperature of 175 °C and initial strain rates of 5×10^{-5}–3×10^{-3} s^{-1}. The ultrafine grain alloy exhibited superplastic characteristics at low temperature. The ultrafine alloy with 0.7 μm grain size achieved 240% superplastic elongation at initial strain rate of 1×10^{-4} s^{-1} [38]. FSP was used to process copper composites that were reinforced with boron carbide particles. FSP was processed with five different tool operating conditions and optical microscopy was used to evaluate the results. The researchers observed that FSP parameters had significant influence on the composite, distribution of reinforcing particles as well as the microhardness of the composite. The boron carbide reinforcing particles had bonded well to the copper composite matrix. In addition, they had a pinning effect on the grains of the copper composite which caused significant refinement in microstructure of the copper surface [39]. Another study used FSP with multiple steps to process an Al-Mg alloy matrix and added SiC nanoparticles. Microscopy was used to examine the dispersion of SiC in stir zone and nanoparticle interaction with the Al-Mg alloy matrix. SiC nanoparticles had significant impact on

the orientations as well as the distribution of the grains. The dynamic recrystallization during FSP processing caused the refinement of SZ grain down to 1.4 μm and sub-grain below 1 μm. In comparison to Al-Mg alloy, FSP processed nanocomposite gained significant more improvement of 140% in hardness, 75% in yield stress and 60% in ultimate tensile strength [40]. FSP was used to process cast Mg alloy to achieve finer grain and higher strength. FSP caused dynamic recrystallisation which transformed the coarse grain into fine grain. For this alloy with high hardness, FSP process dispersed the second phase particles without dissolving them [41]. A study subjected three Aluminum samples with different purity levels to FSP processing to evaluate their grain sizes. Researchers found that an increase in Zener–Hollomon parameter would cause a decrease in grain size. It was demonstrated that the recrystallized grain of 99.999% Aluminum was larger than lower purity 99% and 99.99% Aluminum [42].

FSP processing was used to study the ductility of Aluminum alloys. A low ductility has serious negative effect on the formation and structural integrity of alloys. The researchers demonstrated that FSP processing significantly reduced the ductility degradation in 6056 Aluminum alloy. FSP processing significantly improved the fracture strain of the AA6056 by a factor of two [43]. A study used FSP processing to evaluate the microstructure modification and mechanical properties of 6082-T6 Aluminum Alloy. The researchers used multi-pass FSP processing. The rotational speed was kept constant but three different traverse speeds were applied to FSP process. The higher level of heat generated by multiple FSP passes increased the grain size, dissolved the precipitates, and fragmented the second phase particles. An increase in traverse speed increased the strength and hardness but did not affect the grain size.

A higher rotation of the tool did not affect the tensile strength and hardness of the material but increased the mean grain size in the stir zone [44].

2.2.3 FSP Tools

The FSP process deploys a non-consumable tool that is used to stir the alloys as they are being joined. The non-consumable tool has two types where one has pins and the other is without pin as shown in Figure 2.3 [23].

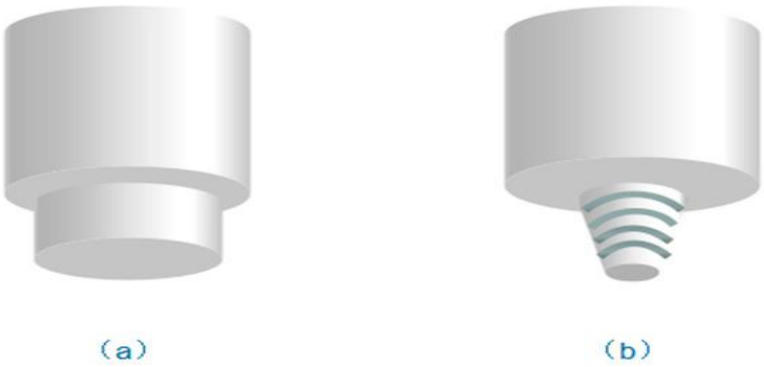

Figure 2.3: FSP stir tools without and with pins [23]

The tool that has pins is used more frequently. The toll without pins is usually used to modify the material surfaces. A study evaluated the microstructure and mechanical properties of enhanced tool steel surfaces using FSP processing. The surface of the steel sample was processed using a tool with no pins under different FSP process conditions [45]. The tool with no pins is also used during composite processing to incorporate reinforced particles [46]. Tool size and pin shape have significant impact on heat generation and material flow as a result of FSP process. A large tool shoulder diameter can generate higher level of heat and cause more significant plastic deformation in the alloy. In such case, the microstructure of the FSP material will be more stable and second phase particles will be refined further [47]. Tool pin design plays an important role in generating heat and friction for effective implementation of plunge stage in FSP process. The researchers investigated different pin shapes such as

conical, square, pentagonal and hexagonal. The results demonstrated that a conical pin generates the lowest temperature in the plunge stage [48].

Researchers investigated the effects of tool size and shape on FSP formation of A1050-H24 Aluminum surface composite by incorporating Silicon Carbide (SiC) particles. The researchers used 3mm, 5mm and 7 mm tool probes. They also used four different tool shapes (circular shape with threads, circular shape without threads, square shape, and triangular shape). The results showed that the square shape incorporated the SiC particles homogeneously in SZ zone compared with other shapes regardless of what rotational speed was used. In addition, the square shape produced finer grains in Aluminum matrix in the SZ zone. However, the wear rate for the square and triangular shapes were higher than circular shape. The probe size had little effect on homogeneity of the SiC particles distribution in SZ. The microhardness of SZ achieved a high level of 60 Hardness Vickers (HV) with square shape after three passes and was stronger than 23 HV for Aluminum matrix outside SZ zone [49].

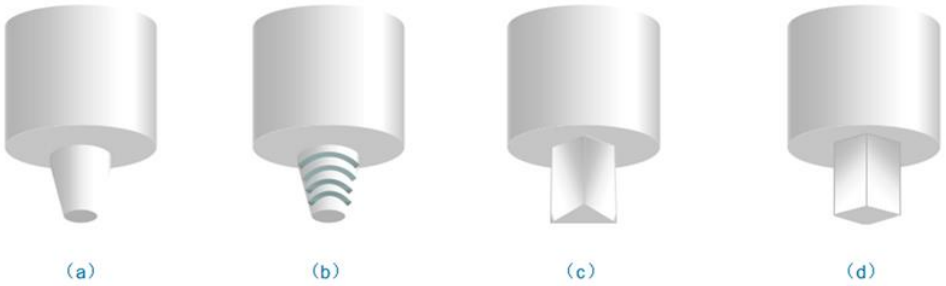

Figure 2.4: Pin shapes: (a) circular; (b) circular with thread; (c) triangular; and (d) square [23]

2.2.4 FSP Reinforcing Particles

FSP processing was developed as a technique to fabricate surface composites. Many researchers have attempted to incorporate reinforced particles to strengthen various

properties in different alloys. In 2003, one pioneering research team successfully distributed SiC particles in Aluminum matrix and fabricated Al–SiC surface composites with strong bonding. The microhardness of the reinforced surface composite was 173 HV which was double the microhardness of 5083Aluminum alloy at 85 HV. The findings of this study were groundbreaking and extremely important for subsequent development of high- performance surface composites [50].

An interesting FSP study was conducted more recently in 2019. A team of nine researchers used both a cone and a pinless tool and incorporated B4C ceramic particles on the surface of AA7075 alloy. The research team experimented with different tool rotation speeds of 400 rpm and 600 rpm. In addition, they investigated higher number of passes designated as 1, 2, 3, and 4 passes. The research team performed detailed analysis on microstructure and microhardness of FSP joints at different depths and studied the wear behavior of the reinforced AA7075 substrate. The researchers concluded that higher number of FSP passes improved the dispersion of the ceramic reinforcing particles. An interesting research finding was that the pinless tool was more effective than the cone tool in dispersing the ceramic particles more homogeneously across AA7075 surface. Another interesting finding was that a noticeable improvement in wear resistance properties of AA7075 workpiece was observed after incorporation of B4C ceramic particles [51].

A wide range of particles have been studied as reinforcing candidates for composites fabricated with FSP process. One example is Zr55Cu30Al10Ni5 bulk metallic glass plate which was successfully welded below the crystallization temperature [52]. Another example is NiTi particles which can incorporate some shape memory into the composite. The results indicated that FSP is effective in fabricating NiTip/Al

composites with good mechanical properties and shape memory [53]. In another study, high-strength chopped E-glass and S-glass fibers were used for reinforced particles with Al1100 Aluminum alloy. The result showed very significant improvement in the mechanical properties [54]. Other researchers used nano-sized TiC powder as reinforced particles on a substrate made of mild steel and performed FSP processing. The results showed maximum 450HV micro hardness which was significantly improved compared to mild steel microhardness of 130HV without reinforced particles [55]. In another research, reinforcing particles of SiC and Al2O3 were incorporated with a cast AZ91 Magnesium through FSP processing. Researchers reported that the microstructure developed with SiC particles had smaller grains and higher strength, elongation, and hardness compared to reinforcing with Al2O3particles [56]. Another research project involved AZ31 which is a widely used Magnesium alloy with Aluminum. The researchers used Direct Friction Stir Processing and designed a pinless and hollow tool that allowed the reinforcing particles to flow through and reach SZ zone. The results showed the grain size of composite layer dropped to 1.24 μm and microhardness doubled to 115.51 Hv [57]. Another group of researchers used high-density polyethylene polymer as the reinforcing particle for FSP processing of AA5059 Aluminum alloy. The results showed significant number of interlocks between the polymer matrix and AA5059 in SZ zone. The researchers observed the formation of ultrafine <100 nm grains which caused a significant improvement in various mechanical properties [58]. Another study in 2014 aimed to demonstrate for the first time that FSP processing can incorporate yttria particles on a copper substrate. The researchers confirmed that yttria powder dispersed evenly within the cooper matrix. Also, the researchers observed that repeated passes of FSP process would cause the powder particles to become finer and disperse more evenly on the copper substrate

surface. The researchers used Transmission Electron Microscopy (TEM) to examine the dispersion of 10 nm powder particles and found no clustering effect and even dispersion in Cu matrix. This study demonstrated that yttria powder used as reinforcing particle improved the strength and hardening properties of copper [59].

In addition to dispersing reinforcing materials on the surface of workpieces, another method is to produce workpieces with a large groove or array of holes pre-fabricated prior to FSP processing. The built-in large groove or the holes are filled with reinforcing particles and the substrate is processed with multiple passes of FSP to manufacture new composites. Figure 2.5 shows pre-fabricated substrates with a built-in groove and built-in array of holes to incorporate reinforcing particles [23].

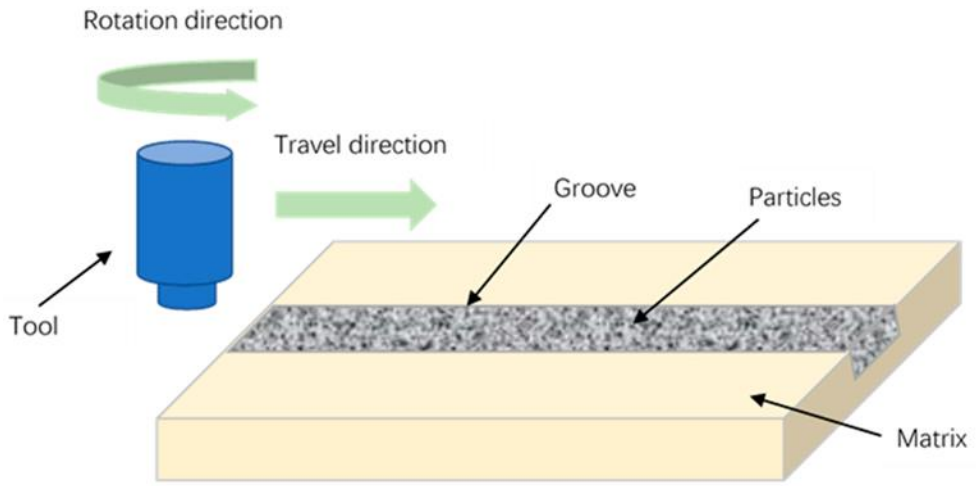

(a)

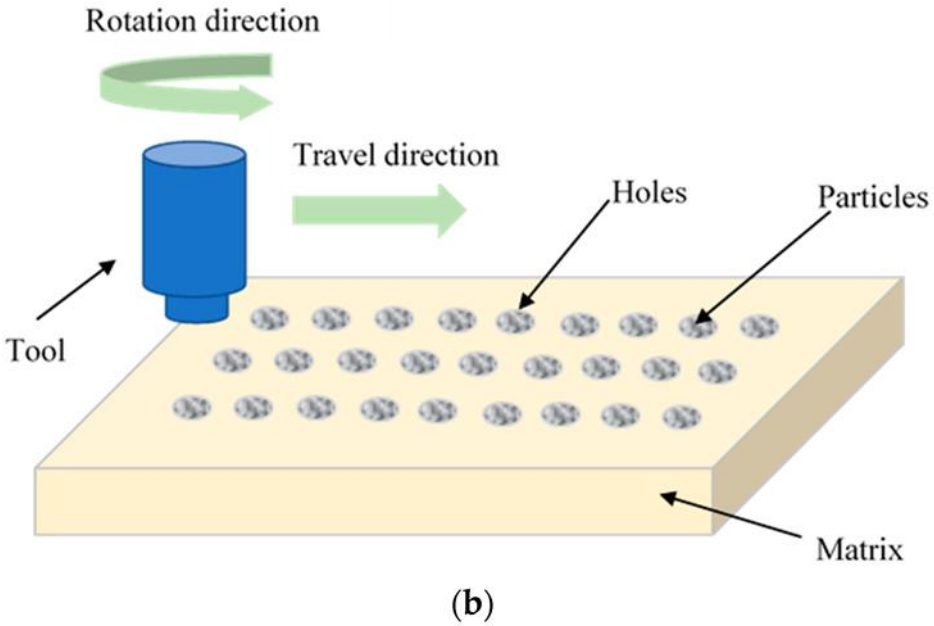

Figure 2.5: Pre-fabricated FSP plates with (a) groove; (b) holes [23]

2.3 Applications of Friction Stir Processing

2.3.1 Development of FSP Superplastic Materials

Superplastic materials are extremely useful in production of sophisticated components in various industries. The conventional techniques for processing superplastic materials are not efficient. The conventional technology can only produce rather coarse grains. As a result, it is only possible to achieve superplasticity at relatively high temperatures if a traditional technique is used. However, FSP technique can achieve superplasticity at low temperatures. FSP processing results in superplasticity through a process that involved grain boundary sliding (GBS) of grains that are fine, equiaxed and misoriented. Researchers applied FSP technique to process a variety of microstructures with different grain sizes and misorientations that resulted in different elongations and stress values. A combination of small grain size and high misorientation creates larger elongation [60,61].

2.3.2 Merging FSP with Other Techniques

Researchers have merged FSP with other processing to combine the advantages of both processes. For example, Selective Laser Melting technique has been utilized in conjunction with FSP processing. A research study demonstrated that lightweight products manufactured with Selective Laser Melting were subjected to FSP for localized surface processing to improve the microstructure of AlSi10Mg parts [62]. In another research, FSP processing was implemented on 70/30 copper nickel substrate that was produced by laser direct metal deposition (DMD). The findings showed that FSP was more effective than DMD in refining the grains, decreasing both the porosity and the ductility as well as increasing the hardness of the alloy [63]. Another research team investigated a variation of FSP process. The researchers used electric current to assist with FSP fabrication of Aluminum AA5083-H111 composite that incorporated Alumina particles dispersed as reinforcing particles. The researchers reported that the use of electrical current FSP variant extended the depth of reinforced layer by 500% and its width by 40%. In addition, the hardness of substrate surface decreased around 10% [64].

2.3.3 Development of New FSP Composites

Different research teams around the world have utilized different reinforcing particles and successfully developed a variety of new composite materials [51, 52, 53, 54, 55, 56, 57, 58, 59]. More research is ongoing to find new composites. More recently, FSP in-situ fabrication of composites has gained a lot of attention. FSP in-situ processing is also referred to as reactive FSP. In the case of in-situ, the types of powders are used that can react with each other or with the alloy matrix during FSP processing. Aluminum composites made with in-situ method are processed more effectively than conventional ex-situ composites. A study in 2011 demonstrated for the first time that

FSP process was able to completely homogenize in-situ distribution of reinforcing particles after two FSP passes. Aluminum-TiC composite was successfully fabricated in-situ with a mixture of K2TiF6 and graphite powders. The grain size was successively refined after each pass which caused significant improvement in mechanical properties. The unique result of this study showed ductility was not degraded and at the same time a far higher strength and hardness was achieved [65].

2.4 3D Simulation of Friction Stir Processing

2.4.1 Modeling of Temperature Distribution

A recent study in 2020 performed Abaqus®/Explicit simulation to create 3D finite element models for the temperature and stress of AA 7075-T651 alloy when subjected to friction stir welding process in plunging, dwelling and traverse steps. The simulation used Arbitrary Lagrangian–Eulerian (ALE) method with adaptive mesh and mass scaling. Two small AA 7075-T651 workpieces were used to reduce the time required for computer simulation. The dimensions used in the simulation model were 60 mm length, 20 mm width, and 4 mm thickness. The study used a tool rotation speed of 1200 rev/min and traverse speed of 2 mm/s. The simulation was done with plunge time of 12.1 seconds, dwell time of 0.2 second, and moving time of 15.2 seconds. Coulomb's friction model was used to simulate the interface contact between the alloy and the tool. The model simulated the material properties as well as heat transfer at various friction processing steps. A mesh of the workpiece was created with a model element size of 0.5 mm in x-y directions. The z-direction consisted of 4 elements. The total number of mesh elements for the workpiece alloy was 38,400 units. In addition, the support back plate was modeled with only one R3D4 mesh element. The researchers validated the finite element model results and also conducted experimental temperature measurements to compare the results. A digital temperature sensor

instrument was used to monitor the temperature history during friction stir process. During the plunge step, high temperature gradient was observed under the pin. The peak temperature was observed at 599°C and was lower than the alloy's melting point. The study concluded that the temperature was distributed in a symmetrical manner across the width of the workpiece during the friction stir welding process. The results also showed that the advancing side had higher plastic strain than the retreating side [66].

Another research study investigated two substrates of AA7075-T6 that were friction stir welded and the process was simulated with Abaqus®/Explicit software. The researchers monitored the effect of temperature variations on material transfer of AA7075-T6 at various stages. The processing temperature has a direct impact on characteristics of material transfer which in turn has a significant influence on thermomechanical properties of the Aluminum substrate. The temperature in this process is below the melting point of the alloy. However, the distribution of the heat is not even and very high temperatures develop at and near the weld joint. For temperature simulation, the material parameters used were mass, conductivity, and specific heat. The friction heat in this study was loaded using the Dflux subprogram of Abaqus®/Explicit software. Heat flux was used to develop the heat model. The researchers classified the friction process into three stages of initial, stable, and final stage. The peak temperature in initial stage was 380.8 °C and 477.3 °C in the final stage. The research findings showed the material transfer rate would increase as the process would transition from the initial to the final stage. Also, AA7075-T6 material near the weld surface would move toward bottom, the material in the middle of weld would move up, and material in bottom of the weld would barely move [67].

2.4.2 Modeling of Thermo-Mechanical Properties

The researchers of a study in 2019 used their previous 3D model for thermo-mechanical stress analysis and developed a new 3D model. For the new model, Abaqus® Explicit software was used for thermo-mechanical analysis of joining two AA 2024-T3 substrates with friction stir welding process. The model was realistic and included two substrates, a backing plate and a welding tool to simulate real-world objects. The model also accounted for heat generation and transfer during the friction stir process as well as the heat loss in the surrounding environment. The model simulated the plunge period, the dwell period, and the welding period. However, the model did not simulate the tool extraction. The model used mass scaling technique and Arbitrary Lagrangian-Eulerian adaptive mesh technique which ensured high-quality finite element numerical analysis. The model was simplified to reduce the cost of processing the simulation on the computer. The quality of the mesh determined the accuracy of this model. This study used two different mesh types with one more coarse and the other developed for weld zone. The result was that a model using Abaqus® version 6.9-EF1 did not completely simulate every step of the friction process. However, improvements were made on the previous 3D model to develop more accurate simulation for early friction process stages involving plunge, dwell and start of tool rotation. The new model is able to better simulate thermo-mechanical properties. In addition, the new model demonstrated that the shape and geometry of the tool has critical effect on friction stir process. Also, this study proved that the accuracy of 3D simulation results depends on developing a high-quality mesh representation as well as assessment of heat transfer during the process [68].

A research study in 2018 used Abaqus® Explicit software and developed a new thermomechanical model to simulate plunge, dwell, and traverse steps in friction stir

process for joining AA2219-T87 Aluminum alloys. The researchers used Johnson-Cook model to analyze the deformation. The Abaqus® Explicit finite element model simulated AA2219-T87 workpiece and the tool's pin as shown below.

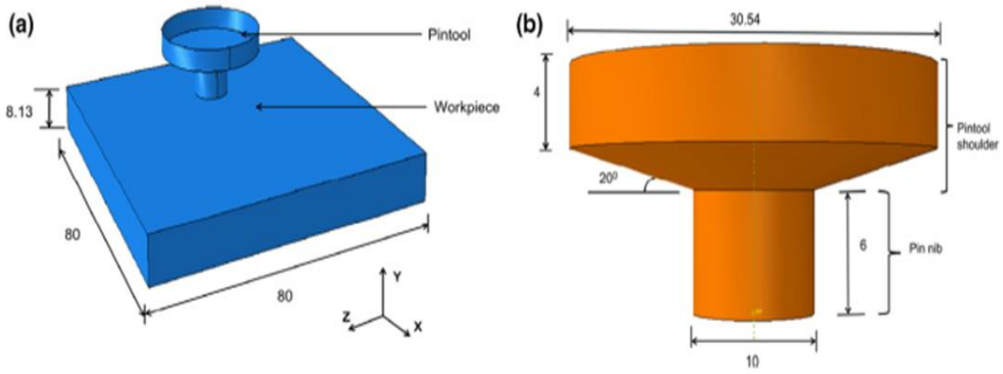

Figure 2.6: 3D model of (a) workpiece, (b) tool pin dimensions [69]

The model included thermal boundary and mechanical boundary conditions. The study modeled the AA2219-T87 workpiece with C3D8RT elements that have eight nodes in 3D. Also, the model used rigid shell element to simulate the tool pin. For simplification of numerical analysis, the researchers reduced the workpiece length and width but kept the thickness value. The model used Arbitrary Lagrangian-Eulerian (ALE) technique and the adaptive meshing for the whole workpiece. Coulomb's friction law was used to represent the shear stress resulting from sliding and a modified version was modeled for simulation. The study showed that friction energy increases almost linearly with the increase in rotation speed. The higher rotation speed causes more plastic deformation. The simulation used different plunge rates of 0.3 mm/s, 0.4 mm/s, and 0.6 mm/s and the depth of plunge was kept at 6.08 mm. The result showed lower plunge rate generated more friction energy and increased the maximum temperature. The rotation speed was simulated at constant rate of 350 rpm and speed of welding was simulated at 1.27 mm. The heat generated during friction stir process was

measured. It was observed that almost 90% of the heat was due to the friction between the workpiece and the tool. The remaining 10% heat generation was caused by the workpiece plastic deformation. The difference between the simulated temperature model and experimental measurement was small at below 4%. The result showed close agreement between the temperature profile of the model and actual experiment as shown below.

The highest plastic energy in this study was observed when both the rotation and welding speeds were increased. The researchers made some simplifications including the use of rigid elements for tool simulation to make the Abaqus® model run faster and reduce the cost of computation. Despite the simplifications, the results of simulation profiles were close to the experimental profiles. This study proved Abaqus® software can accurately simulate the thermo-mechanical properties of friction stir welding process [69].

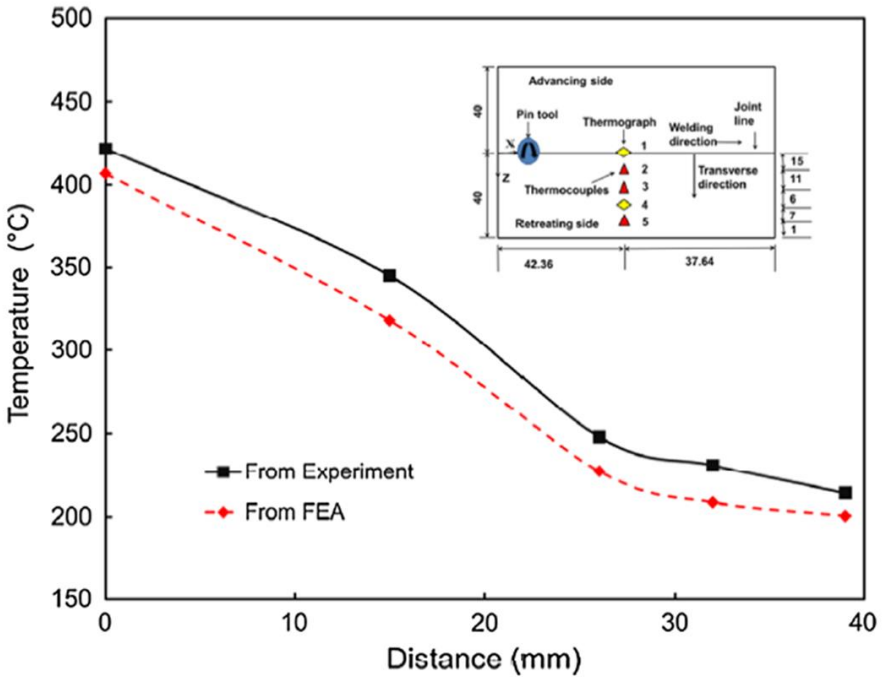

Figure 2.7: Temperatures in Abaqus® model vs experiment [69]

2.4.3 Multi-Pass Modeling of Friction Stir Processing

A study in 2019 simulated multi-pass friction stir processing for Magnesium AZ91 alloy. The researchers developed 3D numerical model using Abaqus® Explicit with Johnson-Cook method to investigate the material flow and plastic deformation. For mesh development, Arbitrary Lagrangian-Eulerian (ALE) technique was used. The researchers discussed friction stir processing is very complex and creation of a 3D model to simulate FSP was very challenging. A 3D model was successfully developed which simulated the effects of two-step FSP process during the tool plunging and stirring stages. The simulation results of the study were close to experimental measurements of researchers. The simulation showed that temperature in advancing side was higher than the temperature in retreating side of the tool. The numerical analysis proved that at end of FSP process when the tool is retrieved, the area surrounding FSP keyhole experiences very high stress rate [70].

2.4.4 Coupled Eulerian-Lagrangian Modeling of Material Flow

Multiple research studies have shown that the use of Coupled Eulerian-Lagrangian (CEL) technique is the most efficient method to model severe plastic deformation in friction stir process. A study in 2019 developed an efficient 3D model to simulate FSP processing for AA5083 Aluminum alloy. The model was developed by Abaqus® Explicit software with Coupled Eulerian-Lagrangian (CEL) technique. CEL was chosen because this technique is well suited for complex flows of materials and can also process severe distortion of 3D mesh without premature termination of computer simulation. The researchers performed multiple simulations with different tool rotation speeds from 600 rpm to 1200 rpm and four types of pin shapes. The results of the simulations were then compared to results from experiments to validate the findings. The study concluded that tool rotation speed was critical in determining temperature,

strain, etc. CEL model accurately simulated the material flowing through the mesh and Abaqus® simulation was efficient [71].

Another research study used Coupled Eulerian-Lagrangian (CEL) technique in Abaqus® CAE software to develop numerical simulation to represent friction stir welding process for AA6082-T6 alloy. Johnson-Cook materials method and Coulomb's friction method were used. Abaqus® CAE was selected because it is better suited for simulating the welding step during friction stir welding process. The study concluded that Coupled Eulerian-Lagrangian technique was powerful and effectively modeled the large deformations that occurred during the welding process in the study. The experimental measurements of processing temperatures proved that the model results was in close agreement with experiments [72]. Another study investigated friction stir processing of marine grade AA5083 aluminum alloy and used Coupled Eulerian-Lagrangian (CEL) technique in Abaqus® Explicit software.

This model was developed to analyze temperature changes during processing by changing the FSP input parameters. In addition to developing the 3D model, the researchers conducted a number of experiments to validate the model at various rotation and translation speeds. The researchers found the difficult task of modeling severe plastic deformation was hard to do with Lagrangian method but was achieved by using the Coupled Eulerian- Lagrangian method. The model was successful in predicting the peak temperatures associated with different rotation speeds. Also, this model successfully simulated the variations in temperature profiles of the advancing side and the retreating side of FSP tool [73].

Another study utilized the Coupled Eulerian-Lagrangian technique in Abaqus® Explicit and developed 3D simulations of material flow and material defects that were formed during friction sir welding process of AA6061 Aluminum alloy. The model simulated the effect of welding process parameters and the shape of tool pin on the flow of material and the formation of voids and defects. The simulation results were verified by experimental measurements. The model predicted the shape of the plasticized zone and detected the voids. However, the size of the voids was overestimated by this model. Another conclusion was that the size of the void was directly impacted by the input parameters. The smaller void size is caused by higher tool rotation or by lowering the welding speed. Another important finding indicated a tool pin with surface features can generate more plastic velocity and material flow as well as reduce the size of the defects more effectively than a tool pin with a smooth surface [74].

2.4.5 Modeling of Complex Curved Surfaces

There has been a significant increase in industrial applications that require friction surface welding to be performed on curved alloys. The 3D models can effectively simulate the perpendicular movement of the tool pin during linear traverse on flat workpieces. However, it is more challenging to model the tool's traverse path along a curvature.

A study was published in 2020 which proposed a new solution for perpendicular tool positioning in 3D thermomechanical analysis and modeling of a complex curved surface. The researchers used both Abaqus® Explicit and Altair Hyperworks® to demonstrate the flexibility of the proposed new method to run on different software platforms. Arbitrary Lagrangian-Eulerian technique was used for creating the mesh elements without distortions. The model was developed with two sections. One section

of the model was a sine function and a separate section was the tool simulation which was programmed to start at the designated welding point on the curved plate. The mesh was C3D8RT brick with 8 nodes and thermally coupled. Two surfaces were defined to accurately represent the FSW contact condition. Four FSW processing steps were defined as plunging, dwelling, traverse, and tool withdrawal. Different rotation speeds and different traverse speeds were used in the model. The material mostly flowed around the pin on the retreating side. In the plunge step, the highest temperature reached by Abaqus® was 300 °C and the Hyperworks® model reached 338 °C which confirmed the temperature was stable during this step. At start of the welding step, temperature reached 531 °C and stayed almost constant until the end of the step. The pattern observed in heat-affected zone was influenced by the shape of the tool pin as shown in Figure 2.8. The researchers successfully developed a 3D model for a complex curved plate [75].

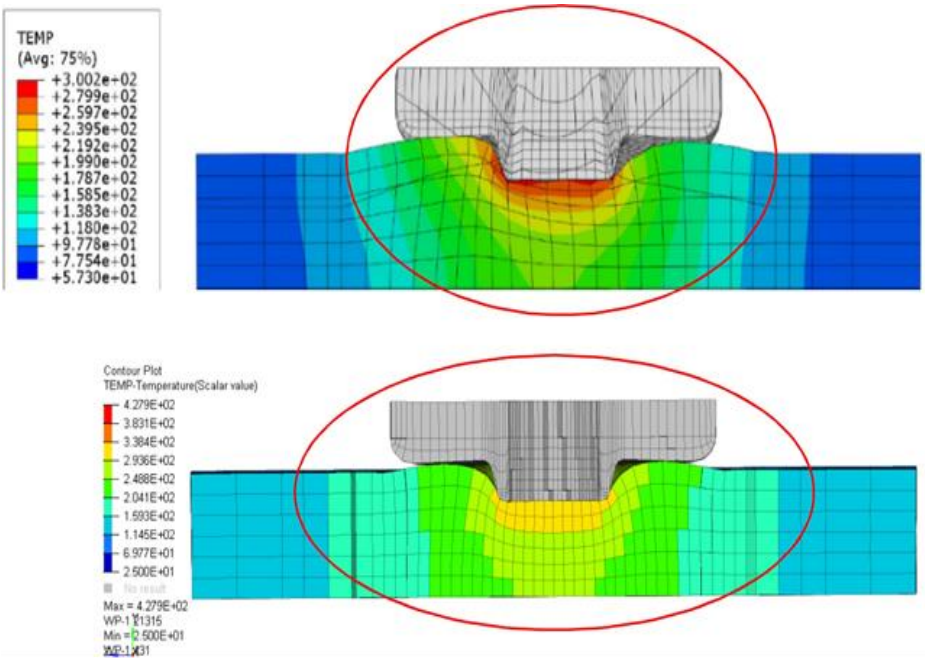

Figure 2.8: Curved model temperature Abaqus® (top) Hyperworks® (bottom) [75]

Chapter 3

METHODOLOGY

3.1 Materials used in 3D Simulation

Two identical AA7075-T6 Aluminum alloy workpieces were used for simulation by Abaqus® Explicit CAE software under six different rotational speeds as well as six different traverse linear speeds. The dimensions of 60 mm x 30 mm x 5 mm were used for both workpieces in this study. The tool pin penetration was simulated at 4 mm into AA7075-T6 workpiece thickness of 5 mm. The tilt angle of the tool pin was set at 2.5 degrees. The chemical composition for the workpiece alloy used in this analysis is shown in Table 1.1. Also, the mechanical properties of AA7075-T6 Aluminum alloy simulated in this study are shown in Table 1.2. Some additional thermo-mechanical properties of the simulation alloy are shown in Table 3.1[76].

Table 3.1: AA7075-T6 thermo-mechanical properties [76]

Property	Value
Melting Point	477-635 ˚C
Thermal Conductivity	130W/m-k
Structure of Crystal	FCC
Electrical Resistivity	5.15e-006 ohm-cm
Machinability Rating	70%
Shear/Rigidity Modulus	29.6 Gpa

AA7075-T6 Aluminum workpieces and the friction stir processing (FSP) tool were modeled by Abaqus® Explicit elastic and plastic materials. A diagram with simulation of the two workpieces is shown in Figure 3.1.

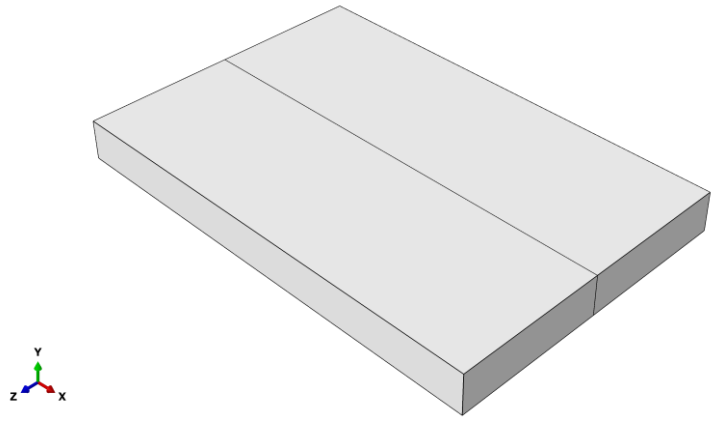

Figure 3.1: Simulated diagram of workpieces in present study

The starting dialog box for Abaqus/CAE 2017 software used in the present study is shown in Figure 3.2 [77].

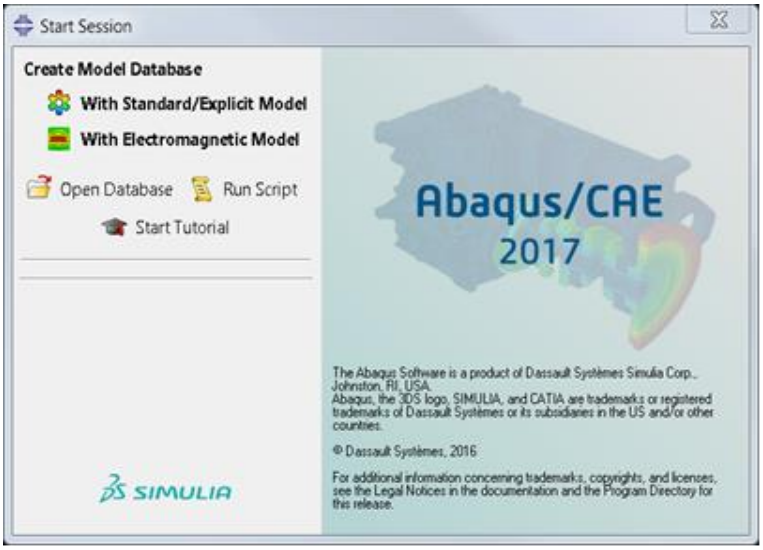

Figure 3.2: Abaqus® start dialog box [77]

In the present study, a coupled Eulerian-Lagrangian simulation method was used. The tool pin was modeled using the Lagrangian method and the two Aluminum AA7075-

T6 workpieces were modeled using the Eulerian method. The tool shoulder and pin simulated with Abaqus® is shown in Figure 3.3.

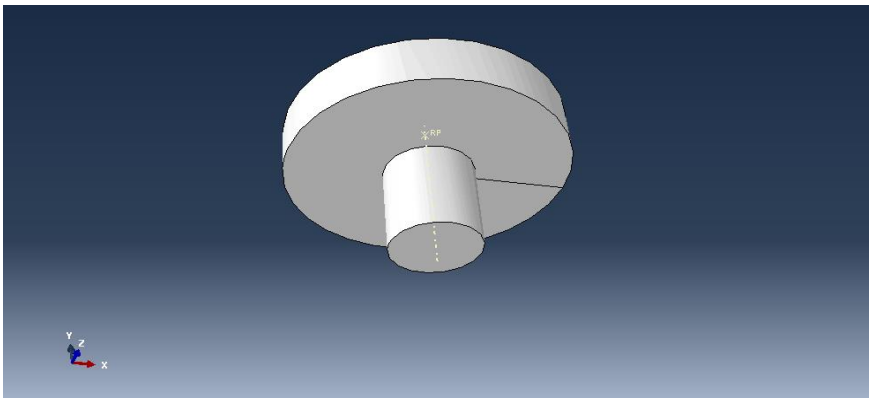

Figure 3.3: Simulation of tool shoulder and pin

The simulated assembly system with two workpieces and a tool is shown in Figure 3.4. The Abaqus® feature with fixed edges for the same assembly FSP bonding system are shown in Figure 3.5.

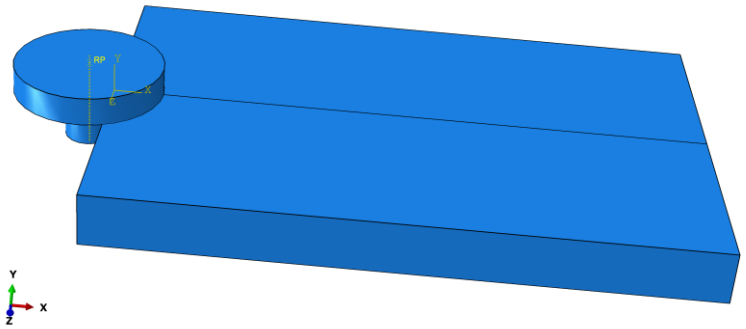

Figure 3.4: Abaqus® assembly FSP bonding system

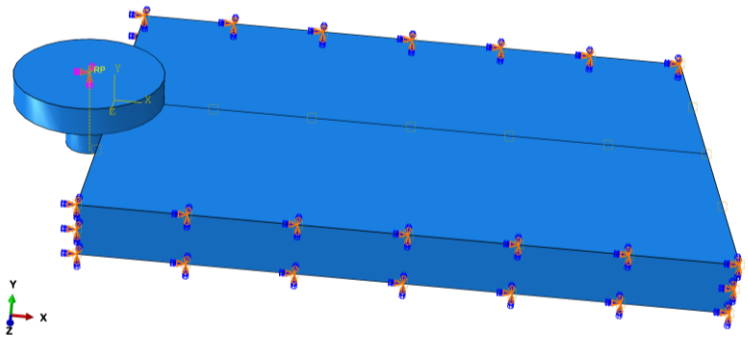

Figure 3.5: Abaqus® workpieces with fixed edges

The corresponding coupled Eulerian mesh for workpiece exterior surfaces and Lagrangian mesh for tool exterior edges are shown in Figure 3.6.

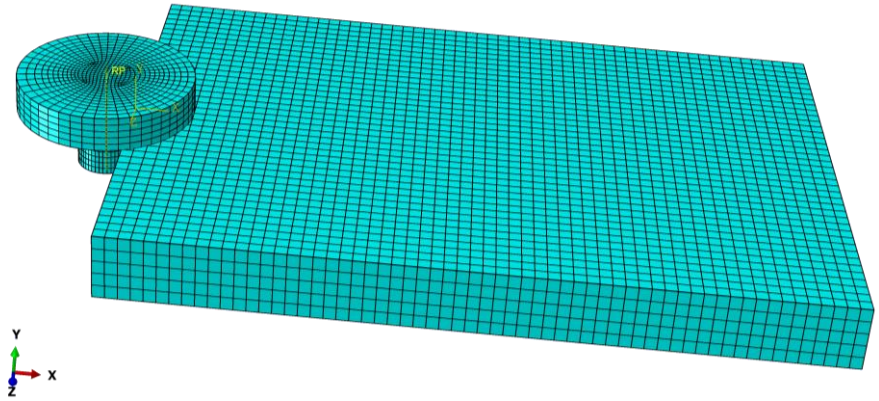

Figure 3.6: Coupled Eulerian-Lagrangian mesh

The numerical finite element analysis in the present study treats the tool as a Lagrangian component and the two AA7075-T6 workpieces are treated as Eulerian components as shown in Figure 3.7.

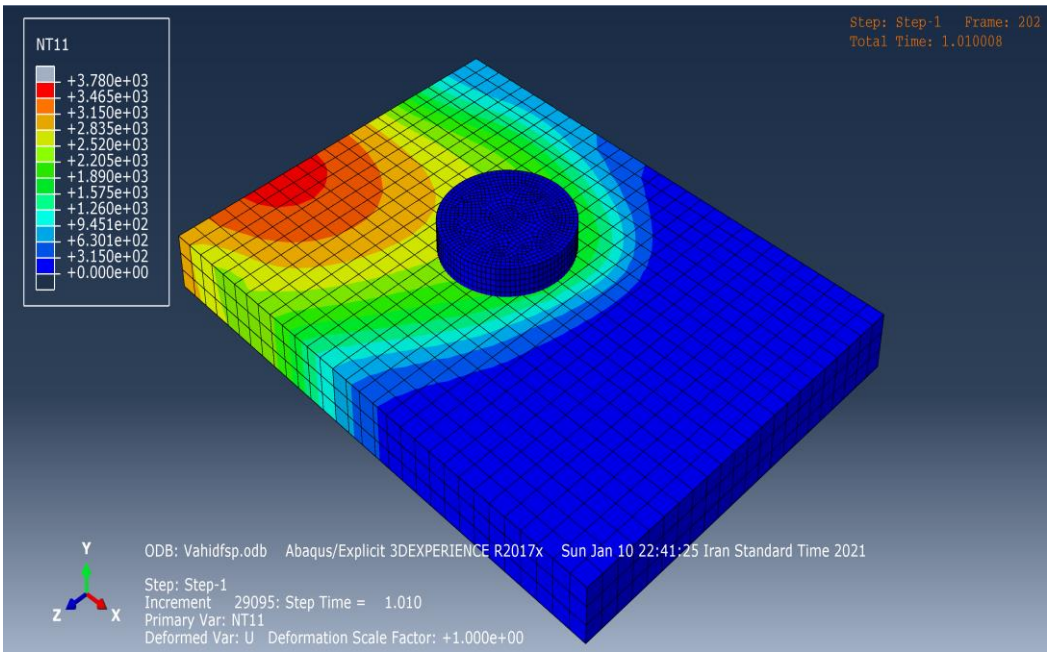

Figure 3.7: Lagrangian tool mesh and Eulerian plate mesh

3.2 Eulerian Finite Element Analysis of AA7075-T6 Workpiece

The present study has used the Eulerian finite element analysis to analyze AA7075-T6 Aluminum workpiece in Abaqus® Explicit within Abaqus®/CAE modeling environment. The present study simulated two AA7075-T6 Aluminum alloy plates joined by friction stir processing. Johnson-Cook technique was used for modeling the material flow behavior at high temperatures. The Abaqus® Explicit algorithm used here contains a built-in model of Johnson-Cook.

3.2.1 Overview of Eulerian Technique

In a pure Eulerian simulation, the workpiece materials are allowed to flow across element boundaries in a rigid mesh. In contrast, other simulation techniques such as Lagrangian would define the materials to be closely associated with an element. The other models would only allow the materials to move as a result of the deformation of the mesh which leads to element quality issues in their deformable mesh. Eulerian simulation does not cause any element quality problems. Therefore, Eulerian method

can be used for simulation of material damage and deformation in the workpiece. Eulerian technique can only be implemented in Dynamic, Explicit steps [78].

3.2.2 Eulerian Numerical Analysis of Workpiece

In Eulerian method, the interaction between the surfaces of adjacent workpieces is set to perfect bonding as a default value. The Eulerian technique is well suited for machining applications due to large plastic deformation, material failure, and the tool contact with workpiece. It is challenging task to simulate a machining application [79].

3.3 Eulerian Workpiece Modeling in Abaqus®/CAE

The present study selected the Eulerian model for the Aluminum workpiece because it is well suited for any application which involves an extreme level of deformation that results in fluid flow.

The elements defined in a Eulerian model can analyze severe plastic deformation of the workpiece more accurately than the elements defined in other models that experience distortion and inaccuracy. The Eulerian technique is also well suited to model the workpiece material penetration problems which is important in friction stir processing. Eulerian simulation elements are flexible and can be empty, partially filled, or completely filled with material. This means the material boundary should be calculated at each point in time. Also, the material boundary does not need to match to element boundary. The mesh elements are usually rectangular and are designed to expand more than the material boundaries. The extra space allows room for the simulated material to flow and deform. The Eulerian workpiece simulation does not account for any materials that flow outside the mesh [80].

Abaqus®/CAE Visualization module was used in the current study to display and analyze the AA7075-T6 Aluminum alloy surfaces. Modeling the contact surface is

critical for FSP process because the main source of heat is from friction between the contacts. The “surfaces” in Abaqus® are used to define the contacts and interactions between materials or the regions of distributed surface loads in a user-friendly manner. In addition, Abaqus® surface tool allows the dissimilar meshes of two or more dissimilar alloys to interface with each other which is very useful for accurate simulation of real-world material interaction and flow. Surface application can be used to model and analyze mechanical, thermal, and thermo-mechanical interactions between similar and dissimilar alloys. Abaqus® surface software can define the faces, edges, and ends for both rigid and deformable elements. Abaqus®/Explicit software has capability to define the Eulerian material surfaces and material contact algorithms. Abaqus®/CAE tool is user friendly and most modeling operations such as material geometry selection are done with a few clicks of the mouse. In the present study, the contact pair between two AA7075-T6 Aluminum alloy workpieces was defined by selecting faces on geometric part instances. Each face was converted into a surface for the input file and Abaqus®/CAE designated a name for the workpiece surface [81].

3.4 Eulerian Surface Definition of Workpiece

The present study used the Eulerian surface application within Abaqus®/Explicit Software to simulate the exterior surfaces of two AA7075-T6 Aluminum alloys.

The Eulerian surface by definition is three-dimensional (3D) and defined with model data. The workpiece materials in Eulerian analysis are simulated as flowing through their corresponding Eulerian mesh. Unlike other simulation models, the Eulerian surface model is complex. It is not possible to define the Eulerian surface with a simple list of element faces. The Eulerian surfaces must be computed at each point in time because they are usually located inside the Eulerian elements. To define any workpiece surface using the Eulerian technique, the name of the material instance must be

specified for the model and defined through Eulerian section application. Abaqus®/Explicit software can compute the exterior boundary for any material instance and can also create a surface that represents that boundary. As the material deforms over a time period, the Eulerian surface application computes the workpiece surface at each point in time. The name of the material instance in Eulerian model should be specified to define a surface. The material instance names are specified in Eulerian section definition. Table 3.2 shows the Eulerian surface definition is selected In Abaqus®/Explicit [82].

Table 3.2: Abaqus® Eulerian surface definition [82]

Input File Usage
SURFACE, TYPE=EULERIAN MATERIAL,
NAME=name
material instance name,

3.5 Eulerian Element Definition for Workpiece Deformity

Eulerian elements application within Abaqus®/Explicit was used in the present study to simulate severe deformation of two AA7075-T6 Aluminum alloys. AA7075-T6 workpiece deformation was simulated using the classical Johnson-Cook model that is available as a built-in feature of Abaqus®/Explicit. The Eulerian elements are only available for the explicit analysis.

Eulerian model elements are optimized for simulating the workpiece materials that are subjected to severe deformation. The Eulerian technique allows the deformed materials to flow from one element to the next element even if the corresponding mesh was fixed. The Eulerian model elements are EC3D8R (3D 8-node element) and

EC3D8RT (3D 8-node thermally coupled element). The two-dimensional (2D) simulations can be estimated by one-element thick mesh with a well-defined boundary delineation. The Eulerian mesh consists of a simple rectangular element array and the shape is different from the Eulerian materials. The Eulerian method can accommodate very complex material configurations inside the workpiece mesh. The Eulerian technique is flexible and can use elements that are completely full or less than full in the vicinity of empty and void spaces. The section definition is a list of materials that are allowed to reside inside the Eulerian elements. The section properties for Eulerian elements must be defined by assigning the section to its corresponding elements. This set of elements must not share nodes with other types of elements. Table 3.3 shows the Eulerian section defined in Abaqus®/Explicit [83].

Table 3.3: Abaqus® Eulerian section definition [83]

Input File Usage:
EULERIAN SECTION, ELSET=element_set_name
Data lines giving list of materials
Abaqus/CAE Usage:
Property module: Create Section:
Select Solid as the section Category and Eulerian as the section Type
AssignSection:
Select part

3.6 Eulerian Element Library

Abaqus®/Explicit contains a library of elements used in Eulerian 3D analysis the AA7075-T6 workpiece in the present study. The distributed loads for element-based loading were only available for analysis of the Eulerian elements. All the elements

used in the analysis were required to have eight nodes to enable proper 3D simulation. The sequence and order of the Eulerian nodes and face numbers are shown in Figure 3.8 [84].

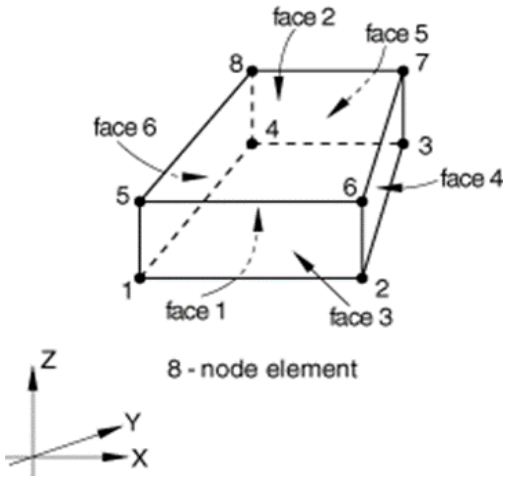

Figure 3.8: Eulerian node orders and face numbers [84]

The faces of Eulerian elements are defined in Table 3.4 [84] and the types of elements available in Eulerian model are shown in Table 3.5 [84].

Table 3.4: Definition of Eulerian element faces [84]

Face 1	1 – 2 – 3 – 4	face
Face 2	5 – 8 – 7 – 6	face
Face 3	1 – 5 – 6 – 2	face
Face 4	2 – 6 – 7 – 3	face
Face 5	3 – 7 – 8 – 4	face
Face 6	4 – 8 – 5 – 1	face

Table 3.5 Abaqus® Eulerian element types [84]

Eulerian stress/displacement element: EC3D8R
8-node linear brick, multimaterial, reduced integration, hourglass control
Active degrees of freedom: 1, 2, 3
Eulerian thermally coupled element: EC3D8RT
8-node thermally coupled linear brick, multimaterial, reduced integration, hourglass control
Active degrees of freedom: 1, 2, 3,11
Nodal coordinates required: X, Y, Z

These elements were used in the present study. In addition, the present study used output variables as AA7075-T6 for Eulerian material instance as defined in the Eulerian section application. The Eulerian technique automatically assigned the output variable names to AA7075-T6 Aluminum alloys. Because the present study uses two AA7075-T6 alloys, material instance names were defined as “AA7075-T6” and “AA7075-T6” and stress output was requested from the Abaqus®/Explicit program. The Eulerian model then assigned two separate stress component variables named “S11_ AA7075-T6” and “S11_ AA7075-T6”. The Abaqus®/Explicit program provides all output variables of Eulerian analysis in format of global coordinates [84].

3.7 Eulerian Mesh Model for AA7075-T6 Workpiece

In the present FSP study, two workpieces of AA7075-T6 aluminum alloy were jointed together under Eulerian simulation. The same dimensions of 60 mm x 30 mm x 5 mm were used for both workpieces. The tool pin penetration was simulated at 4 mm. These dimensions were deemed appropriate for FSP processing but not considered too large to complicate the Abaqus® Eulerian computational run times. The workpieces were used to analyze the friction heat generation and heat loss of TMAZ zone during the FSP process. The temperature generated during FSP process was less than the melting temperature of AA7075-T6 Aluminum alloy. The temperature distribution in the present study during FSP process was not steady in the stir zone (SZ) and heat-affected zone (HAZ). The temperature was uneven with higher temperature around the joined surfaces. For creation of the AA7075-T6 workpiece mesh, ultrafine elements were used to represent the material around FSP joint surfaces to develop an accurate Eulerian model. The present study used the same ultrafine elements to represent AA7075-T6 surface areas in the rest of the workpiece plates away from the two joining surfaces. The present study prioritized computational accuracy and used extra-long run

times. As a result, there was no attempt to reduce the Eulerian computational complexity and cost by using coarse mesh in regions farther away from the two joined surfaces. Approximately 20,000 nodes and 15,000 elements were used for the Eulerian mesh representation of two AA7075-T6 Aluminum alloy plates in the present study.

3.8 Heat Transfer Model

The two AA7075-T6 workpieces used in the present study provided a good opportunity to analyze the heat generation and heat transfer of FSP process under realistic conditions. The material parameters that had critical importance for heat transfer analysis were thermal conductivity, specific heat, and alloy mass. The density of AA7075-T6 aluminum alloy used in the present study was 2810 kg/m^3. The thermal conductivity was 130W/m-k. The specific heat of AA7075-T6 was 960 J/kg °C at the start of the FSP processing with a temperature of 25 °C. The present study simulated the tool rotation at different speeds of 135 rpm, 500 rpm, 1000 rpm, 1500 rpm, 2000 rpm, 2500 rpm. Also, the feed rate was simulated at linear speeds of 16 mm/min, 25 mm/min, 50 mm/min, 75 mm/min, 100 mm/min and 125mm/min. Also, the tilt angle of the tool pin was set at 2.5 degrees. The depth for penetration of tool pin into the workpiece was specified at 4 mm. The movement of tool rotation was set to the clockwise (CW) direction.

The heat in the present study was generated from two friction stir processing (FSP) sources and were modeled accordingly. Both the tool pin and the tool shoulder generated heat in the heat-affected zone (HAZ). The surface heat model was used for the tool shoulder. Also, the volume heat model was applied to the pin tool thermal analysis. The temperature variations were simulated throughout the FSP process in the initial stage, the middle stage, and the final stage at the end of joining the two plates.

The gap radiation application in Abaqus®/Explicit was used to model the heat exchange between the two AA7075-T6 surfaces that were placed next to each other. Abaqus®/Explicit was also used to analyze and model both the distributed heat flux and the surface heat flux. However, only the EC3D8RT type elements were supported by this software. The Eulerian analysis in Abaqus®/Explicit had an important application called "Thermal Loads" which was used for analyzing the heat transfer and temperature displacements of AA7075-T6 workpiece in the present study. Table 3.6 shows the types of thermal loads that were used in the present analysis [85].

Table 3.6: Abaqus® Eulerian types of thermal loads [85]

Concentrated heat flux prescribed at nodes
Distributed heat flux prescribed on element faces or surfaces
Body heat flux per unit volume
Boundary convection defined at nodes, on element faces, or on surfaces
Boundary radiation defined at nodes, on element faces, or on surfaces
Moving or stationary heat fluxes defined in user subroutine UMDFLUX

In the present study, the heat flux was not uniform due to FSP processing. The VDFLUX subroutine in Abaqus®/Explicit was used to define the nonuniform flux distribution in the present thermal analysis. VDFLUX subroutine was used to specify the variations in distribution of flux as function of FSP temperature, tool position, FSP processing time, rotation speed and linear speed. An example of the user interface with VDFLUX subroutine is shown in Table 3.7 [86].

Table 3.7: Example of Abaqus®/explicit VDFLUX [86]

```
Subroutine vdflux

C Read only (unmodifiable)variables -

1 nblock, ndim, kStep, kIncr, stepTime, totalTime, jUid,

2 amplitude, temp, curCoords, velocity, dirCos, jltyp, sname,

C Write only (modifiable) variable - 1 value )

C include 'vaba_param.inc'

C dimension curCoords(nblock,ndim), velocity(nblock,ndim),

1 jUid(nblock), dirCos(nblock,ndim,ndim), temp(nblock),

2 value(nblock) character*80 sname

C do 100 km = 1, nblock

user coding to define value 100 continue

return

end
```

Chapter 4

RESULT AND DISCUSSION

4.1 Overview of the Study Results

The present study simulated all the critical stages of plunging, dwelling, and traverse that occurred during the FSP processing of two identical workpieces under different rotation and linear traverse speeds. The main goal of the present study was to investigate the elastic-plastic thermo-mechanical behaviors in joining two identical AA7075-T6 Aluminum alloys using the friction stir process. Figure 4.1 shows the workpiece dimension of 60 mm x 30 mm x 5 mm entered on Abaqus®/Explicit.

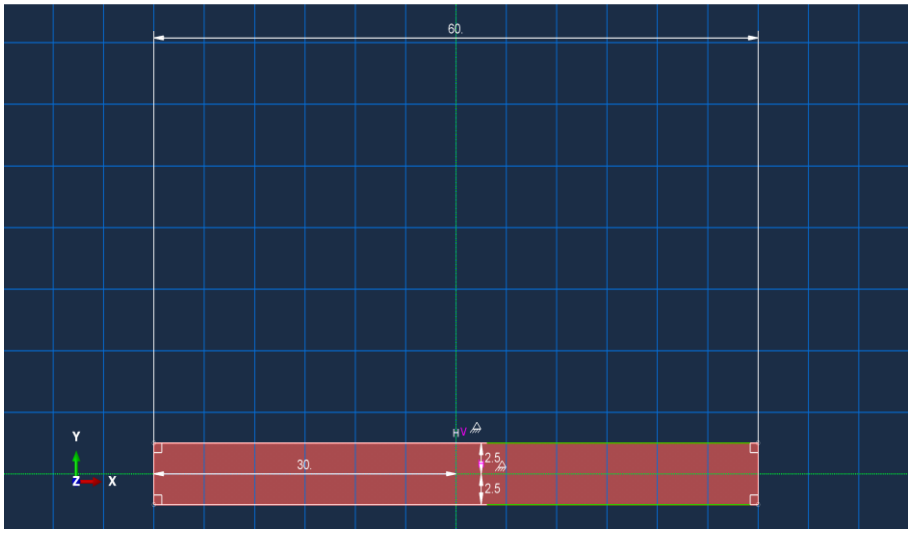

Figure 4.1: Dimensions of two workpieces on Abaqus®

FSP processing was successfully simulated with proper friction and plastic deformation results. It was found that the temperature distribution and the mechanical effects were directly interrelated. The present study accounted for heat and plastic

deformation generated from friction as well as the effect of higher temperatures on FSP mechanical properties. The FSP region that experienced the most plastic deformity was the thermo-mechanical-affected zone (TMAZ). The study simulated the changes in material properties as a result of temperature increase and the impact on plastic deformation, friction, and thermal evolution of AA7075-T6 workpiece.

4.2 Results of Thermal Simulations

The present study successfully developed a finite element model for investigating the FSP process parameters such as heat generation and temperature transition of AA7075-T6 workpiece over the region where the two faces were joined. The present study used Abaqus®/Explicit to simulate heat transfer from the beginning step of tool plunging to the next step of dwelling and then the traverse and the final FSP step. Figure 4.2 shows the temperature transition at two distinct points in the FSP process.

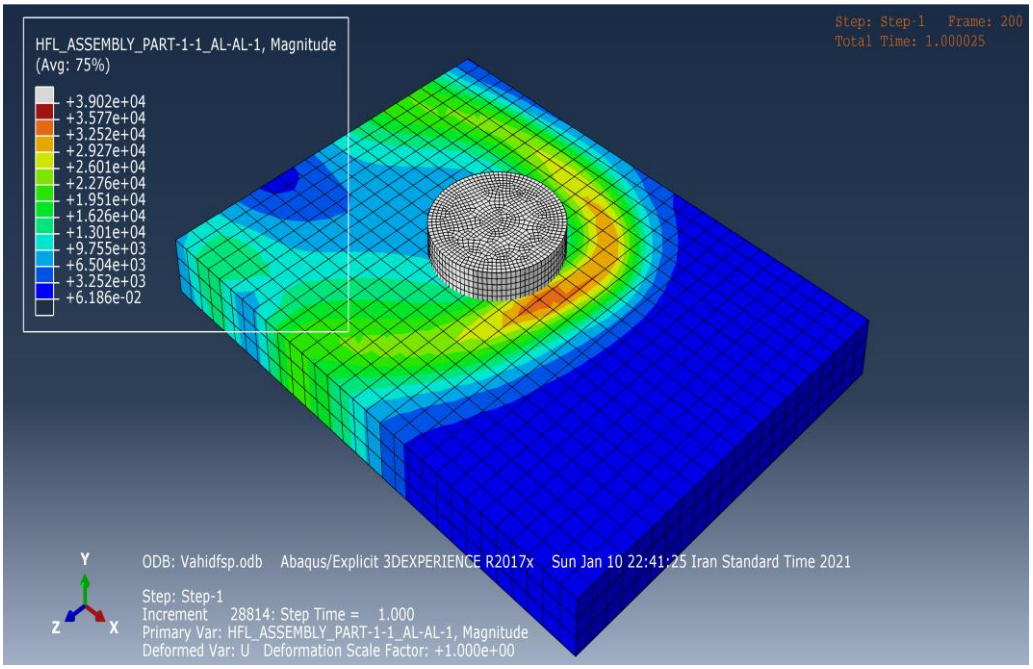

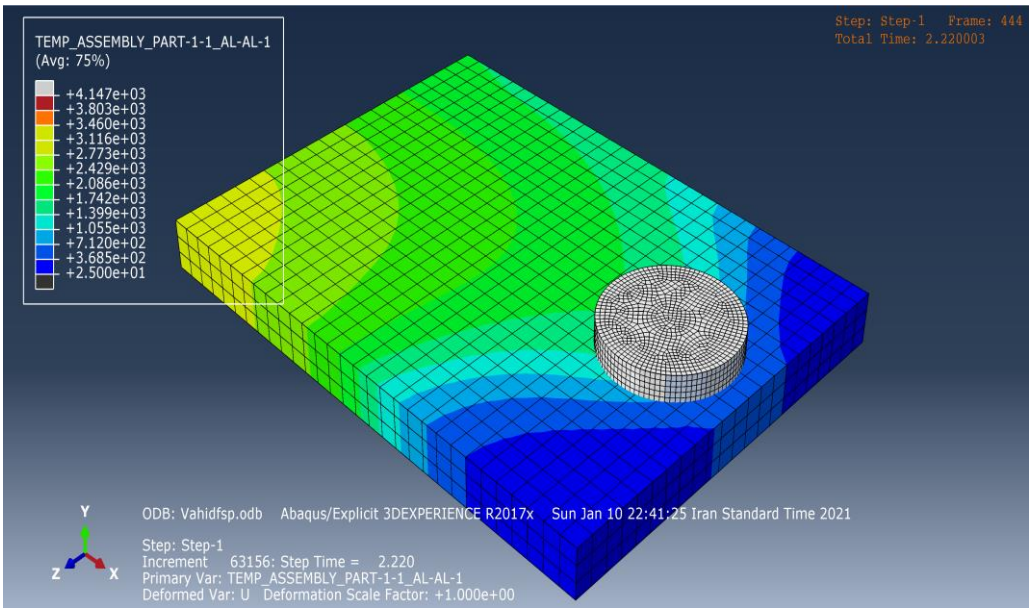

Figure 4.2: Examples of temperature transitions

FSP heat is distributed across both the bonding joint traverse path as well as in perpendicular angle to the direction of FSP traverse path and across the two work plates on both sides of the joint path. A cross-section of the workpiece is the best way to demonstrate the heat penetration into the thickness of the workpiece around the tool pin as well as the temperature distribution generated by the FSP process which is actually a three-dimensional heat distribution across both plates being joined. As explained above, Figure 4.2 indicated temperature transition across some of the workpiece surfaces in the present study. The heat generated by the FSP process is at the highest level around the center of the FSP joining path. As the distance from FSP centerline increased outward and closer to the perimeter side of the two workpieces, the temperature dropped across the cross-section toward the edge of the workpieces on both sides. The temperature dropped outward across SZ, TMAZ, HAZ zones until the points located in the area of base metal BM region farthest away from the FSP joining path in the center of the FSP stir zone (SZ). Figure 4.3 below presents both the mesh model for the cross-section of the workpiece as well as the FSP temperature distribution across AA7075-T6 alloy.

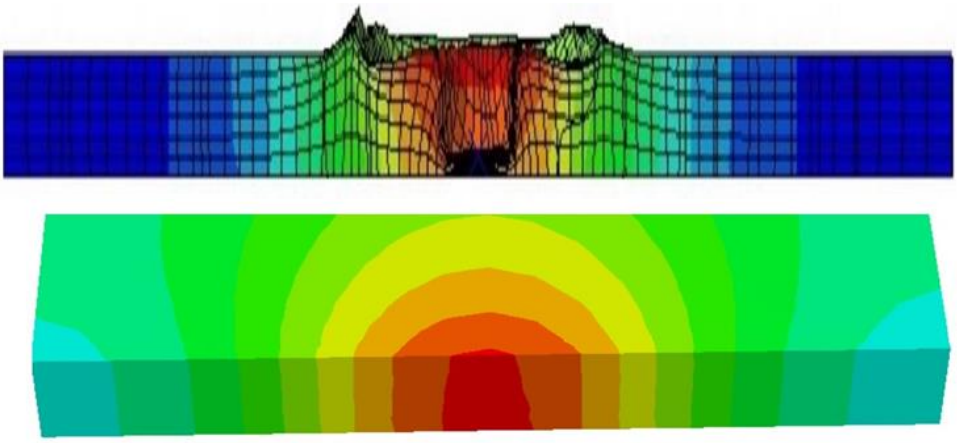

Figure 4.3: Cross-section of temperature distribution

As indicated by both Figure 4.2 and Figure 4.3, AA7075-T6 workpiece temperature distribution is three-dimensional and extends into the workpiece thickness side in both workpieces that are joined by FSP process. The heat transition at each point during FSP process was calculated by a subroutine in Abaqus®/Explicit which determined the flux at each point. The result of Eulerian workpiece simulation showed significant temperature increase in the region directly beneath the contact area between the tool pin and AA7075-T6 surface at the start of tool plunge and penetration. The temperature gradient continued to varying degree as the FSP process continued. Also, the workpiece surface displayed semi-circle contours representing different temperatures as shown in Figure 4.2. Thermal model simulation showed a steady increase in the temperature at each area along the FSP path until the tool shoulder made contact with the area. At that point in time, the workpiece surface region adjacent to the tool pin experienced highest temperature reading. One of the interesting findings of this study was that the maximum thermal result was achieved when the model simulated a full contact between the Eulerian representation of the AA7075-T6 workpiece and the Lagrangian representation of the FSP tool. The simulated maximum temperature stayed well below the melting point of AA7075-T6 alloy. At the next point in time, FSP temperature dropped a little and basically stayed steady for the rest of the FSP

processing. The 3D algorithm simulated the tool as it transitioned from plunge step, moved along the traverse path and eventually joined the two alloys. The thermal profile as simulated by the Eulerian technique stayed stable throughout the FSP process. The simulation demonstrated thermal stability even at the time of workpiece softening and material flow.

The temperature distribution and FSP processing relationship was based on the location of the point where the temperature was measured as well as its distance from the FSP joint center line. Temperature distribution was stable in the middle of the plate along the bonding path and was measured at around 335 °C peak temperature. However, toward the end of plate, the temperature increased significantly and reached more than 400 °C because the surface and thickness areas had small room left for heat to dissipate so the temperature kept rising above 400 °C. Also, it was noticed that as the distance from the FSP joint centerline increased, the temperature across the plate decreased. In addition, temperature distribution was three dimensional and spread across both the surface and the thickness of AA7075-T6 plates. Another interesting finding of the present study was that the temperature transition was almost symmetrical between the FSP advancing and retreating sides at the time instant the model simulated a full contact between the Eulerian representation of the AA7075-T6 workpiece and the Lagrangian representation of the FSP tool. The simulation results which are basically symmetrical imply that the direction of tool rotation does not have much effect on thermal profile of the FSP joint. Although an experimental validation was not performed in the present study, the present finite element simulation was considered as reasonably accurate representation of real world FSP process. The reason is that FSP process did not generate enough heat to bring AA7075-T6 to the melting point. Therefore, the thermo-mechanical properties and material flow were

kept under reasonable boundary control which enabled successful Eulerian and Lagrangian modeling for FSP process with reasonably high accuracy.

It should be emphasized that the user subroutine in Abaqus®/Explicit was extremely useful for flux calculations to evaluate the heat transfer and thermal transitions during the entire FSP process from the beginning step to completion of AA7075-T6 joint. The performance of Abaqus®/Explicit in modeling the heat transfer was very impressive despite the effects from many factors including plunging speed, workpiece heat loss in SZ zone, heat transfer from the workpiece to the back plate, several transitions in temperatures throughout the FSP process especially the frequent shifts in the maximum temperatures across the path of FSP joint.

In the present study, Abaqus®/Explicit was used to create the models for both the temperature distribution as well as the important parameters of AA7075-T6 that absorb heat distribution such as material stress and strain rate. The model for the strain distribution indicated somewhat of symmetrical shape under the effect of FSP bonding temperature. The simulation model showed mechanical stress and strain at cross-section of the FSP bonding joint. The stress in the alloy joint was caused by a combination of mechanical and thermal effects. The tool pin rotation in the stir zone causes the high strain rate and FSP friction generates the heat. The residual stress and material strain were the most important FSP parameters related to the temperature distribution in this study. Abaqus®/Explicit model was able to take into account the effects of both stress and strain as a result of the FSP temperature distribution as shown in Figure 4.4 below.

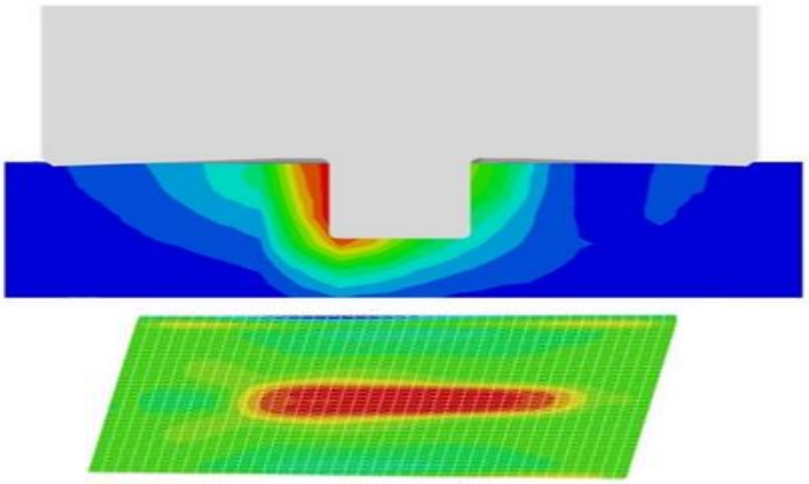

Figure 4.4: Stress and strain relationship to tool pin and heat distribution

4.3 Results of Mechanical Simulations

In mechanical simulation of the present study, the effects of thermal transitions on AA7075-T6 were modeled as function of both the time and the temperature. Figure 4.5 shows computer screen shot for entering the mechanical inputs for the simulation model in the present study.

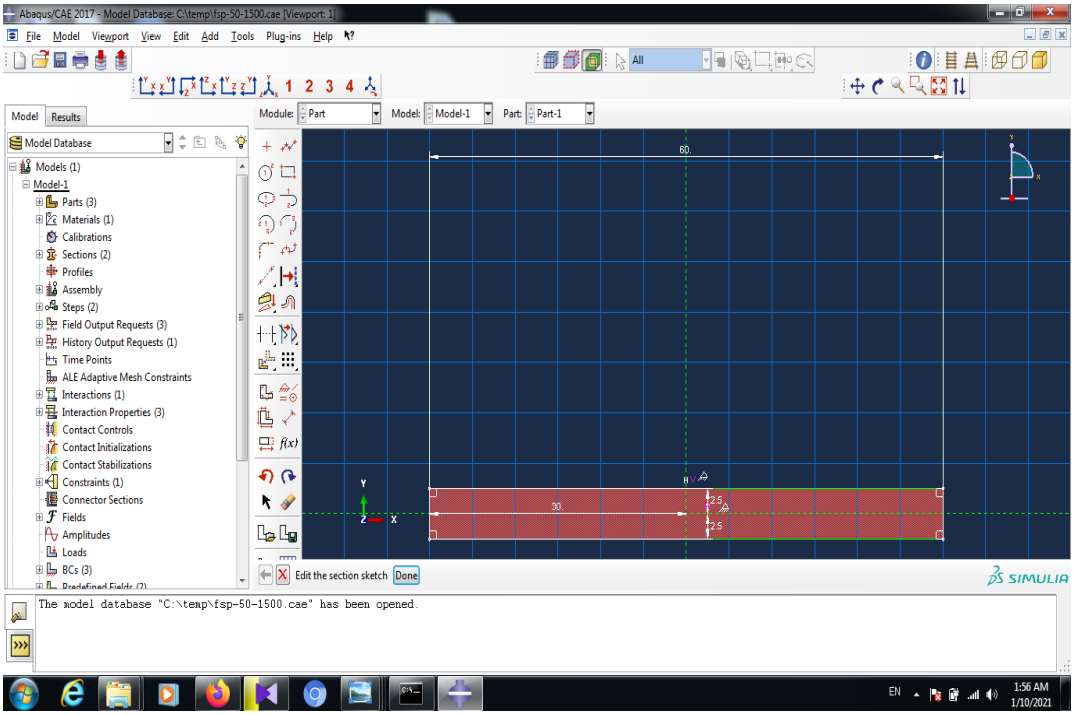

Figure 4.5: Inputs to simulation model on Abaqus®

FSP thermo-mechanical properties were simulated for temperature evolution, heat distribution, stress, strain, plastic deformation, hardness, tensile, and wear. A built-in material softening model within Abaqus®/Explicit estimated AA7075-T6 yield strength as function of temperature. In general, variation in the yield strength was observed as the temperature increased during FSP processing of AA7075-T6 joint. The material behavior of Aluminum alloy workpiece transitioned from the initial room temperature at the start of simulation until it reached high temperature below the melting point of AA7075-T6 and became soft. There were also changes of workpiece material yield strength observed in simulations that corresponded to different peak temperatures that were generated during FSP. Aluminum yield strength values decreased to lower values as temperature values increased. Therefore, AA7075-T6 yield strength had an inverse relationship with FSP temperatures.

In the present simulation, the tool was programmed to travel along the FSP path of two AA7075-T6 joining surfaces until it reached the end point. The mechanical model in Abaqus®/Explicit automatically accounted for different strain rates, different stress levels and other mechanical values associated with each Eulerian element node located along the FSP bonding path. Abaqus®/Explicit thermal model and mechanical model worked together to generate the 3D simulation results. One mechanical risk in the 3D simulation was the possibility of material flow defects and FSP joint distortion. The present 3D analysis did not show any simulation of distortion along the FSP bonding path.

Abaqus®/Explicit built-in Johnson-Cook successfully simulated the plastic deformity of AA7075-T6 in the present study. Johnson-Cook model within Abaqus®/Explicit simulated both the rate and the extent of the workpiece plastic deformation. Also,

Johnson-Cook algorithm simulated the corresponding temperatures associated with AA7075-T6 deformation and material flow. Johnson-Cook algorithm evaluated four typical critical parameters in the present study for FSP temperature, material yield strength, strain hardening, and rate of AA7075-T6 deformation. The advantage of Johnson-Cook model within Abaqus®/Explicit was its simplicity to use. In addition, the result of deformity analysis was consistent with temperature transitions in the Aluminum workpiece. As described before, the temperature and the mechanical simulations showed mutual direct effect on each other. The interaction and mutual effect of the thermal model and the mechanical model across the workpiece at two different points during FSP process are displayed in Figure 4.6.

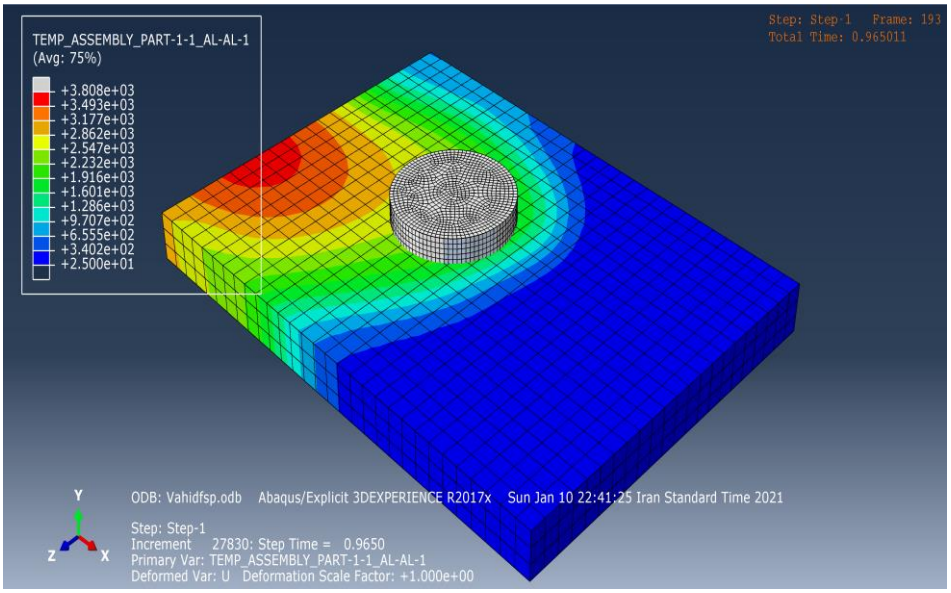

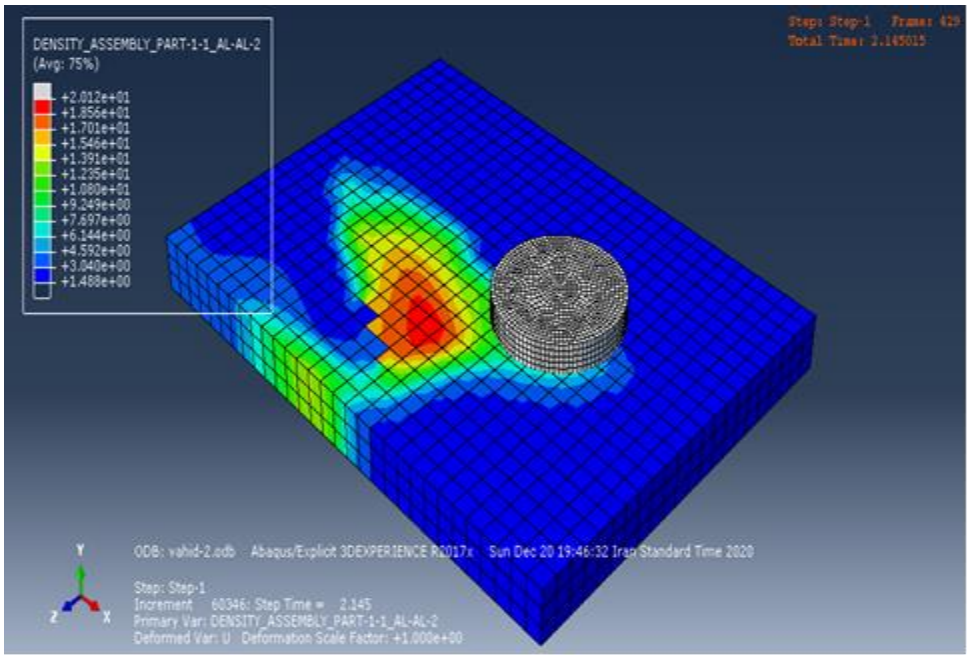

Figure 4.6: Thermo-mechanical changes across workpieces

The present simulation took into consideration both the heat generation from friction and plastic deformation as well as the impact of thermal model on the mechanical model and FSP parameters. The simulation results showed increased stress at start of contact between the workpiece surface and the tool surface below the contact region which is the result of the plunging force of the tool. The stress value also increased in the same area during the dwelling time although it was smaller for the workpiece surfaces outside of tool-workpiece contact area. The depth of tool penetration in the present study was set at 4 mm for simulation of material thickness at 5 mm. As the tool penetrated into the workpiece material, the simulation showed more heat was generated around the region of tool-workpiece contact surface. This resulted in softening of AA7075-T6 which caused a reduction in the material stress simulated within the stirring zone. The simulation results showed later that although the maximum stress point transitioned to another point outside the pin contact area, the material in stirring zone was still experiencing high stress. After the increasing temperatures caused AA7075-T6 to become soft, the material within the stirring zone

was easier to stir. As the material in SZ zone became softer, there was a corresponding reduction in the SZ material stress until it reached a steady value which lasted until the completion of FSP bonding process. The present study demonstrated a strong link between AA7075-T6 alloy temperatures and material stress values. The FSP temperature also had significant effect on the material flow and the quality of bonding between the two AA7075-T6 surfaces. In addition, 3D simulation showed the importance of properly handling the materials in SZ zone to achieve good FSP bonding between the surfaces.

The highest tensile strength (TS) in the present study was estimated at 580 (MPa). The corresponding estimated yield strength (YS) was 450 (MPa). Table 4.1 shows the results for simulated mechanical property estimates for tensile strength and yield strength.

Table 4.1: Results of model for mechanical properties

Rotation Speed (rev/min)	Traverse Speed (mm/min)	Tensile Strength (MPa)	Yield Strength (MPa)
135	16	550	441
500	25	566	444
1000	50	574	447
1500	75	580	450
2000	100	549	439
2500	125	510	412

4.4 Results of TMAZ Zone Simulations

In the present study, the regions near the FSP bonding area and thermal- mechanical-affected zone (TMAZ) were simulated for both the advancing and retreating sides. The simulation included the surface, the middle and the bottom areas of the bonding region. The 3D modeling for TMAZ area is a critical aspect of the present study because the study results are based on the AA7075-T6 material transfer behavior at different points in time during FSP bonding. The material flow and displacement model considered the difference of each point before and after FSP bonding. The present study found almost similar material flow behaviors during different FSP stages. Another important model simulation result showed the material movement direction in TMAZ zone was from the bottom toward the top surface of FSP bonding area. In addition, the present 3D model indicated the tool retreating side was able to consistently displace more AA7075-T6 material in the TMAZ zone compared to the advancing side. An important stage of FSP process occurred at the point when the bonding process stabilized. A vertical force by the rotating tool was applied to AA7075-T6 workpiece and the force magnitude was kept steady as FSP bonding continued. The applied vertical force generated sufficient friction and heat such that plastic deformation was made possible in the workpiece. The effect of heat on the study material created a concave pattern on the AA7075-T6 workpiece. The material flow of FSP bonding was downward from the surface area of the TMAZ zone which resulted in simulated accumulation of some material toward the bottom side of the bonding joint. The simulation in the present study also demonstrated that accumulated material around the bottom of rotating tool in the TMAZ zone was later moved toward the top surface as FSP processing continued.

Another important finding of the present simulation was that AA7075-T6 displacement around the bottom of the TMAZ zone was almost zero. The simulation showed the net effect of both downward and upward TMAZ material displacement resulted in almost zero material transfer around the bottom of TMAZ zone. The lower TMAZ areas with small distance from bottom surface of the workpiece showed little to no movement of AA7075-T6 material. However, material transfer rate increased at larger distances away from the bottom which were located closer to the top surface of FSP bonding region.

The present model for TMAZ zone demonstrated that FSP advancing side experienced a smaller material displacement compared to the retreating side. In addition, there was different peak material displacement values in the TMAZ zone during different FSP stages. The simulation showed that the viscosity of AA7075-T6 decreased as the FSP temperatures increased. As a result, the material region with the lowest temperature experienced the smallest material transfer. On the other hand, the material region with the highest temperature had the biggest displacement. The present analysis showed as more materials accumulated in the bottom of TMAZ zone, the rate of material transfer increased along the traverse path of FSP processing. The simulations showed the material transfer in TMAZ retreating side was smaller during the initial FSP step compared to the stable stage. An interesting finding from the simulation results proved that the highest material transfer occurred during the final FSP stage.

4.5 Effect of FSP in SZ, TMAZ, HAZ Zones

Abaqus®/Explicit simulations of FSP temperatures were largely based on the critical properties of AA7075-T6 alloy which included specific heat, thermal conductivity, and mass. Table 4.2 shows a summary of some AA7075-T6 properties.

Table 4.2: Effect of temperature on workpiece properties

Temperature (^{o}C)	Specific Heat (J/kg ^{o}C)	Thermal Conductivity (W/m ^{o}C)
25	810	130
100	920	140
300	1005	176

The peak FSP temperatures in the present study transitioned across the workpiece at various points around the bonding joint. Figure 4.7 shows an example for a simulated peak temperature on the bonding joint along the workpiece surface.

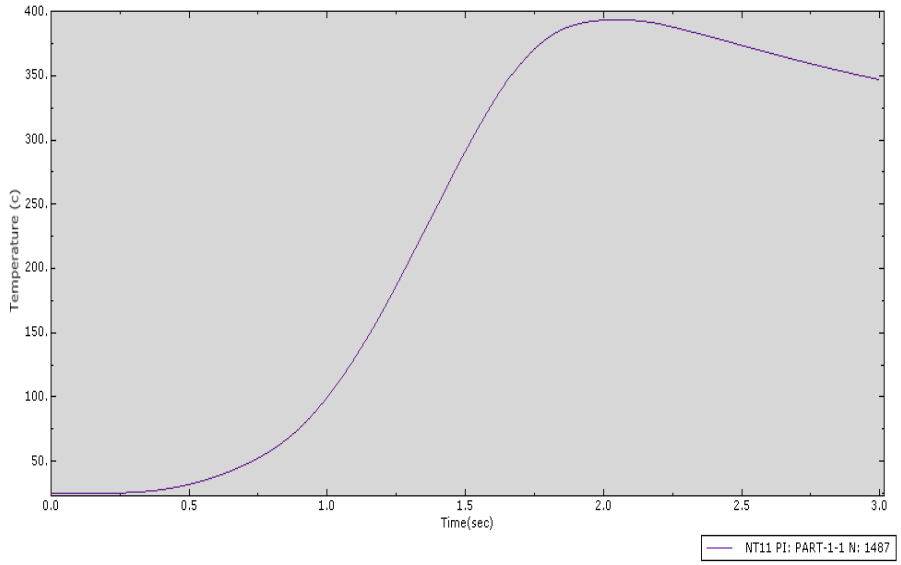

Figure 4.7: Example of simulated peak temperature

Fiction stir processing zones are defined as the stir zone (SZ), the thermo-mechanically affected zone (TMAZ), the heat affected zone (HAZ), and the unaffected base metal (BM). The typical shape produced by the friction stir processing is somewhat symmetrical as shown by the schematic in Figure 4.8 [87].

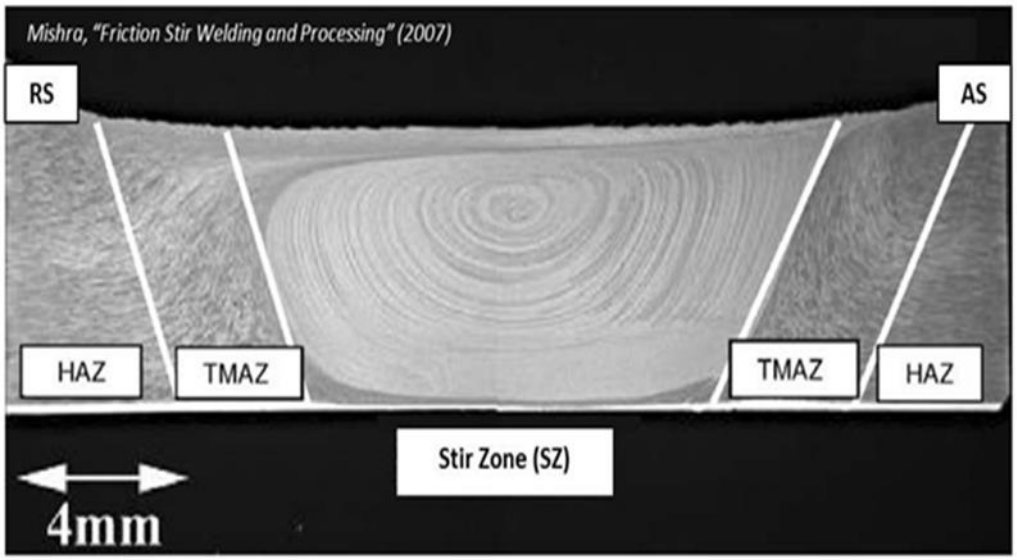

Figure 4.8: Diagram of FSP microstructure zones [87]

The stir zone (SZ) is generally oval-shaped and located in the center as shown in the diagram. The SZ zone is created by the pin of the rotating tool as it softens the workpiece and mixes the bonding materials together. The SZ zone experiences the highest temperature in FSP/FSW processing because it is the region closest to the friction heat generated by the tool pin. The combined effects of high temperature at high mechanical strain causes dynamic recrystallization of SZ grain structure which would produce ultra-fine grain sizes typically in 1 to 10 microns (μm) range [87].

The thermo-mechanically affected zone (TMAZ) is a narrow part of the FSP/FSW region that surrounds the SZ zone. The materials in the TMAZ zone experience the second-highest temperature in FSP/FSW processing at slightly below the temperature of the SZ zone. The combined effects of TMAZ temperature and mechanical strain are not high enough to cause dynamic recrystallization of TMAZ grain structure. However, TMAZ grain structure experiences modification and develops longer grains with different orientation compared to the unaffected base metal (BM) region. The heat affected zone (HAZ) is located outside TMAZ zone and next to the unaffected

base metal (BM) zone in the workpiece. The materials in HAZ zone experience temperature increase but not significant enough to cause deformation. HAZ zone does not experience significant change in its grain size and grain orientation [87].

In the present study, six different tool rotation speeds in revolutions per minute were simulated at 135 rpm, 500 rpm, 1000 rpm, 1500 rpm, 2000 rpm and 2500 rpm. At the start of each of the six rotational simulations, the rotating tool plunged into AA7075-T6 workpiece and dwelled for 2 seconds each time to pre-heat the workpiece for each simulation.

The simulation results showed that as the rotation velocity was increased from the initial 135 rpm to higher speeds, the temperatures increased in the SZ, TMAZ and HAZ zones. The higher temperatures were below AA7075-T6 melting point. At the start of simulation, the temperature of the area around the rotating tool was approximately room temperature around 25 °C. After 2 seconds simulated dwelling time, the simulated temperatures of AA7075-T6 material increased very significantly in the areas surrounding the plunging region of the tool. At the end of 2 seconds dwelling time, the simulated tool rotation started. The rotating tool shoulder and pin started to move along the linear FSP bonding path. In this simulation, the bonding path was close to the linear line but was not perfectly straight along the bonding path. The bonding path simulation can be even more linearized through modification of mesh elements and nodes in numerical simulation.

The heat model in the present study was validated with other studies using the same workpiece material. The increases in temperature due to the increasing tool speeds in the present study was in agreement with the heat results from other studies (66, 67, 89,

90). The simulated temperature measurements on the surface of the AA7075-T6 workpiece in the present study indicated that as the tool rotation and linear movement continued, the simulated temperatures in both SZ and TMAZ started to increase. The simulated temperatures were measured through Abaqus® software at different points on simulated surface. The simulation indicated higher temperatures closer to bonding path compared to areas located father away from the FSP processing joint. However, as the FSP bonding continued along the joint, the rate of increase in the temperature slowed down. The simulation showed temperature was almost steady before the rotating tool reached the middle of the workpiece and increased significantly as simulated tool moved toward the end of the join on the workpiece. An example of a simulated temperature of 335 °C at a point near the stable middle area of the bonding joint measured on the Retreating Side (RS) is shown in Figure 4.9.

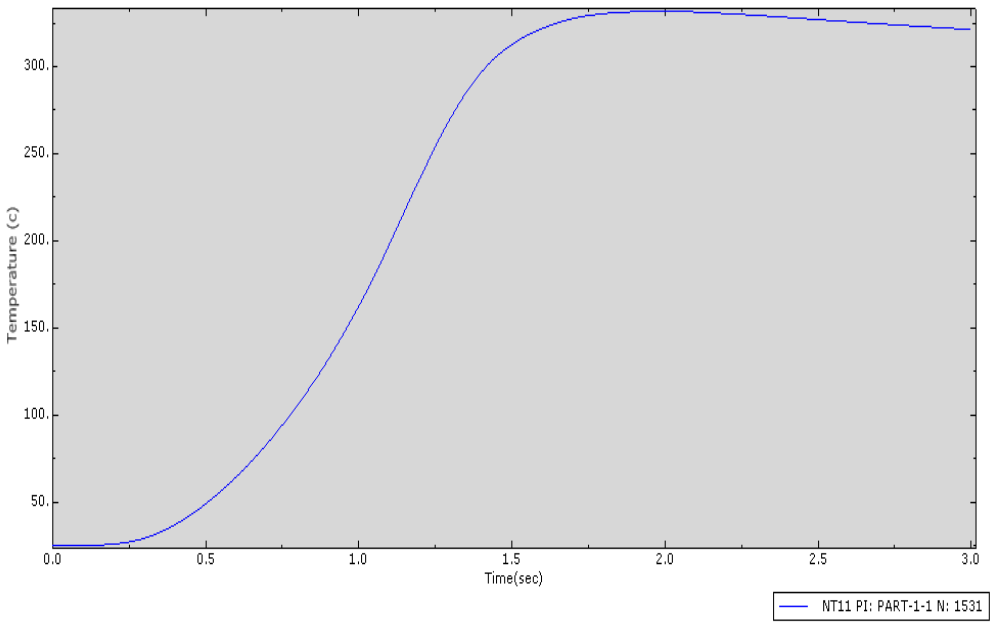

Figure 4.9: Example of simulated temperature

During the time that workpiece temperature was steady, material flow was simulated in SZ and TMAZ zones as was throughout the FSP bonding time.

In agreement with prior research, the simulated peak temperatures increased significantly in the present study as the simulation tool moved toward the end of the workpiece joint. The comparison with other experimental and numerical studies [89, 90] proved that the numerical model developed in current study was able to successfully simulate and predict different FSW bonding path temperatures for AA7075-T6 workpieces. The simulated peak temperature for the present study increased to approximately 440 °C in the region close to end of the bonding joint. Another study reported that high tool rotation velocities and linear traverse speeds may produce stir zone peak temperature as high as 510 °C [75]. However, FSP temperatures are highly dependent on the type of tools and the process parameters used so there is some variation from study to study. A simulated peak temperature near the high-temperature region at the end of the workpiece in the present study is shown in Figure 4.10.

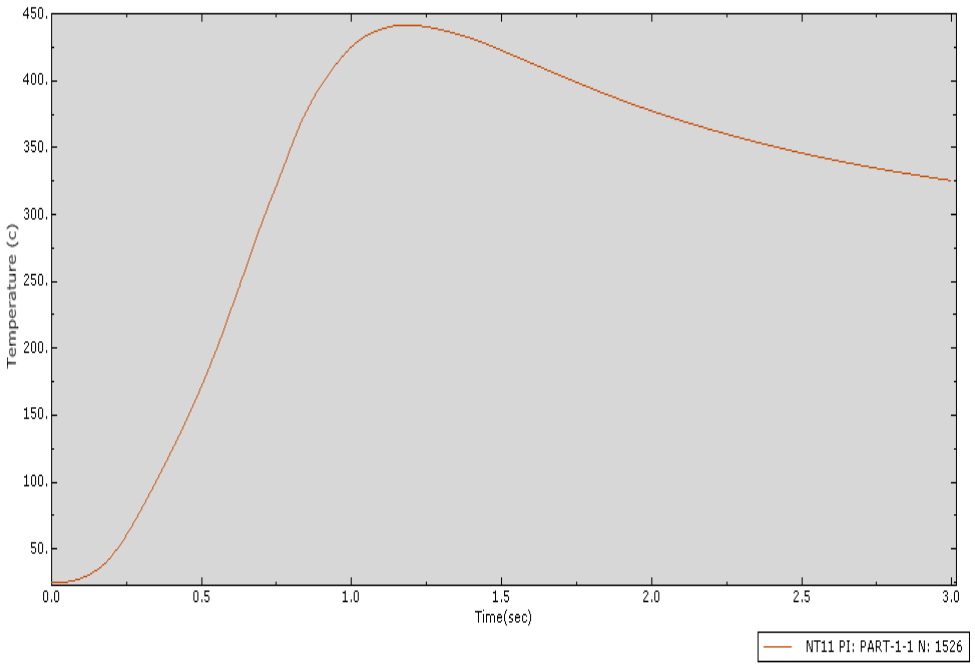

Figure 4.10: Simulated peak temperature 440 °C near end

As the rotational speed increased successively from 135 rpm to 500 rpm, 1000 rpm, 1500 rpm, 2000 rpm and 2500 rpm, material flow generally occurred faster and more AA7075-T6 material was moved in TMAZ zone at higher transfer rate. Also, slightly wider areas were observed in simulations of SZ, TMAZ, and HZ zones. The direction of material transfer in TMAZ was from the bottom of bonding region to the top surface of the workpiece. In agreement with prior studies, the TMAZ material flow movement in the present study was higher in retreating side than the advancing side. As was done in previous research, the present study defined the TMAZ material flow movement as the difference in the distances of a point near bottom of the joint as measured before and after the FSP/FSW processing [89]. The simulation results of the resent study at higher rotation speeds showed that the increase in rate of material flow movement was reduced after rotation was increased above 1500 rpm. The results for simulated material flow movement estimation due to six different rotation speeds is presented in Figure 4.11.

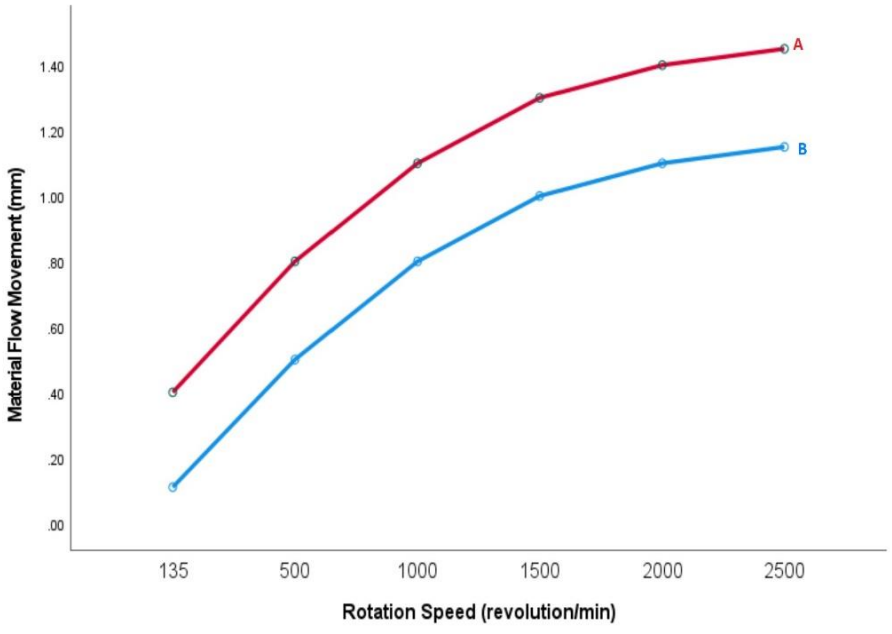

Figure 4.11: Simulated effect of rotation speeds on material flow in retreating side (A) and advancing side (B)

The simulation results were indicative of estimated large material flow in the SZ zones due to the increases in the tool rotation speeds. This result is in general agreement with prior experimental studies [90, 91, 92].

In the present study, the feed traverse rate was simulated under six different conditions at linear speeds of 16 mm/min, 25 mm/min, 50 mm/min, 75 mm/min, 100 mm/min and 125 mm/min. The present study found an inverse relationship between traverse speed and bonding temperature which was consistent with both the experimental and the numerical findings in another study (67). The simulations in the present study clearly showed that lower linear traverse speeds generated higher FSP temperatures on the workpiece. In addition, the inverse relationship found between linear speeds and temperatures in the present study was in agreement with the results of another study that used very high traverse speeds of 1000 mm/min, 2000 mm/min and 2900 mm/min (90). The previous published study reported that increasing the traverse linear speeds at the same rotation speed resulted in lower temperatures around the bonding joint (90). That finding confirmed the inverse relationship simulation result in the present study.

The ratio of rotation speed to traverse speed was very important because it defined the linear distance that the tool pin traveled during each simulated rotation. This ratio was defined as the pitch and was a good indicator for the heat generated as well as the amount of material that could be mixed in SZ zone. The pitch ratio shows the number of revolutions per mm (rev/mm) of linear feed. A proper balance was made between rotation speed and linear speed to generate the right amount of heat for proper optimization of FSP parameters. Too much heat would cause negative impact on the workpiece microstructure and material flow. Too little heat would not create a

successful bonding of the two workpieces. Therefore, the pitch ratio of 20 used in most of simulations in the present study was critical and created the right sizes in SZ, TMAZ, HAZ zones. The pitch ratio of the present study started at 8.4, increased to 20, and then kept constant at 20 as shown in Table 4.3. The ratio used in the present study was in general agreement with other studies which used pitch ratios in the range of 8 to 20 (67), the range of 15 to 30 (91), the range of 17 to 74 (92), and a single ratio of 30 (93).

Table 4.3: Rotation/traverse pitch ratios in the present study

Rotation Speed (rev/min)	Traverse Speed (mm/min)	Pitch (rev/mm)
135	16	8.44
500	25	20
1000	50	20
1500	75	20
2000	100	20
2500	125	20

For each set of rotation and traverse speeds in the present study, the size of SZ zone was simulated to be large enough to create acceptable simulated bonding. The simulated SZ size was not too large so it was expected that defects and voids in the bonded material were avoided in the present simulation. Also, the present model simulated adequate sizes for TMAZ and HAZ zones and reduced the effects of heat and deformation in the workpiece areas that were located farther away from the SZ and bonding path. The results of the present study for simulated material flow movement estimated at six different feed traverse speeds are presented in Figure 4.12.

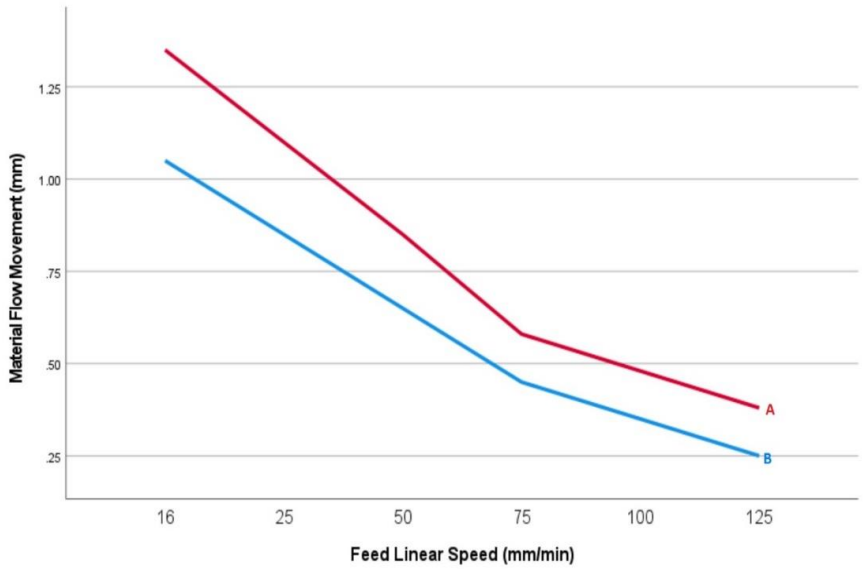

Figure 4.12 Simulated effect of traverse linear speeds on material flow in retreating side (A) and advancing side (B)

In the present study, simulated temperatures were compared across the workpiece and the relative sizes were estimated for the SZ, TMAZ, HAZ zones under different conditions. It was found that increases in the tool traverse speeds from 16 mm/min to 25 mm/min, 50 mm/min, 75 mm/min, 100 mm/min and 125 mm/min caused slightly narrower HAZ zone. Also, small narrowing of TMAZ and SZ areas were simulated with increased traverse speeds. These results were based on comparison of simulated

temperatures measured by Abaqus® at several points on the workpiece surface. In addition, the temperatures in HAZ zone were significantly lower than SZ zone under all six traverse conditions. The simulated temperatures across the HAZ zone decreased further when measured at the simulated surface points located farther and farther away from the bonding joint in the direction of base material (BM). This means that temperatures across HAZ zone decreased as the distance from FSP bonding path increased. The present model simulated significantly higher temperatures in TMAZ and SZ compared to HAZ zone. Figure 4.13 shows an example of a completed single pass FSP simulated with Abaqus®.

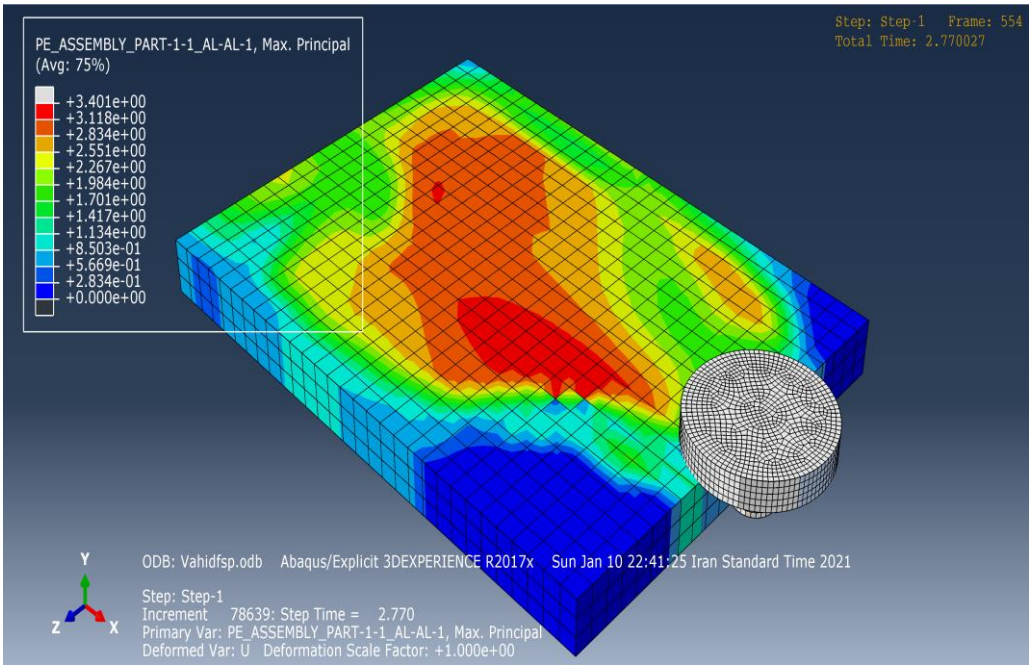

Figure 4.13: Completed single-pass FSP simulation

The TMAZ zone simulation was narrower with lower FSP bonding temperatures generated at increasing feed traverse speeds. In the model developed for the present study, the simulated temperatures on the retreating side (RS) near the bonding path in the stable middle region had an approximate range of 360- 380 °C and with a mean temperature around 372 °C. The temperature decreased in the TMAZ and HAZ zones

at distances farther away from the joint until it reached the base metal (BM) zone which showed no effect. The simulated bonding peak temperature at 16 mm/min linear speed at a point near weld line was 381 °C on the Retreating Side (RS). The corresponding simulated temperature at a point on the opposite Advancing Side (AS) was a little higher than RS side for 16 mm/min feed and its heat measurement was 398 °C. The simulated temperatures in present study under all six traverse speeds showed higher SZ temperature on Advancing Side (AS) compared to Retreating Side (RS) of friction stir processing. These results were consistent with a prior study (93). As the linear traverse speeds were increased, the simulated peak temperatures dropped. For the highest traverse speed of 125 mm/min simulated in the present study, the bonding peak temperature measured near the stable middle section of the simulated bonding path was 362 °C as measured by Abaqus® on the Retreating Side (RS) and 378 °C on Advancing Side (AS). The range was relatively small for the differences in the bonding temperatures of the six different traverse speeds. In addition, the temperatures dropped lower at farther distances located away from the FSP/FSW bonding joint. In addition, the simulated temperatures near the end of the joint were above 400 °C under most of the six feed speeds. This proved that the numerical model in the present study generated enough heat and created six successful FSP joints for the two AA7075-T6 workpieces under six different traverse conditions. These simulated numerical results were consistent with the reported findings from other experimental studies that have investigated the properties of the AA7075-T6 alloy in the past (90, 91, 93).

4.6 Simulated FSP Parameters and Tools

The same dimensions of 60 mm x 30 mm x 5 mm were used for both workpieces in this study. The tool pin penetration was simulated at 4 mm. The tilt angle of the tool pin was set at 2.5 degrees. FSP tool pin encountered high reaction forces in the plunge

step. As a result, the pin material underwent a high stress which affected the tool. The simulation showed high mechanical strength of the tool pin and it was able to handle the high load. The simulation showed that reaction force facing the pin increased significantly as soon as a full contact was made between the pin and AA7075-T6. The magnitude of the reaction force decreased slowly as FSP processing continued to the next stage. As the temperature of the material underneath the pin increased, the reaction force decreased. The simulation results also showed the heat generated by friction was significantly higher than the heat produced by plastic deformation.

The present study simulated the tool rotation at different speeds of 135 rpm, 500 rpm, 1000 rpm, 1500 rpm, 2000 rpm, 2500 rpm. Also, the feed traverse rate was simulated at linear speeds of 16 mm/min, 25 mm/min, 50 mm/min, 75 mm/min, 100 mm/min, 125 mm/min. The depth for penetration of tool pin into the workpiece was specified at 4 mm and the workpiece thickness was simulated at 5 mm. The movement of tool rotation was set to the clockwise (CW) direction.

4.7 Effect of Different FSP Parameters

4.7.1 Parameters of Friction Stir Processing

In the present study, different FSP parameters were simulated and the results were compared under different conditions. The steps involved with the material transfer and the findings associated with different parameters were discussed in the previous section.

As mentioned before, friction stir processing (FSP) is based on the rotation of the tool and the resulting friction and heat that causes workpiece deformation and softening. The first step in friction stir processing is a rotating tool that plunges between two

workpieces that must be bonded together. Two sides are defined for friction stir processing. The advancing side (AS) is defined as the side where direction of tool rotation is the same as tool travel. The other side with opposite direction is called the retreating side (RS). A typical diagram for the friction stir processing is shown in Figure 4.12. The right side of the workpiece in Figure 4.14 is the advancing side (AS). The left side of the workpiece in Figure 4.14 is the retreating side (RS) [88].

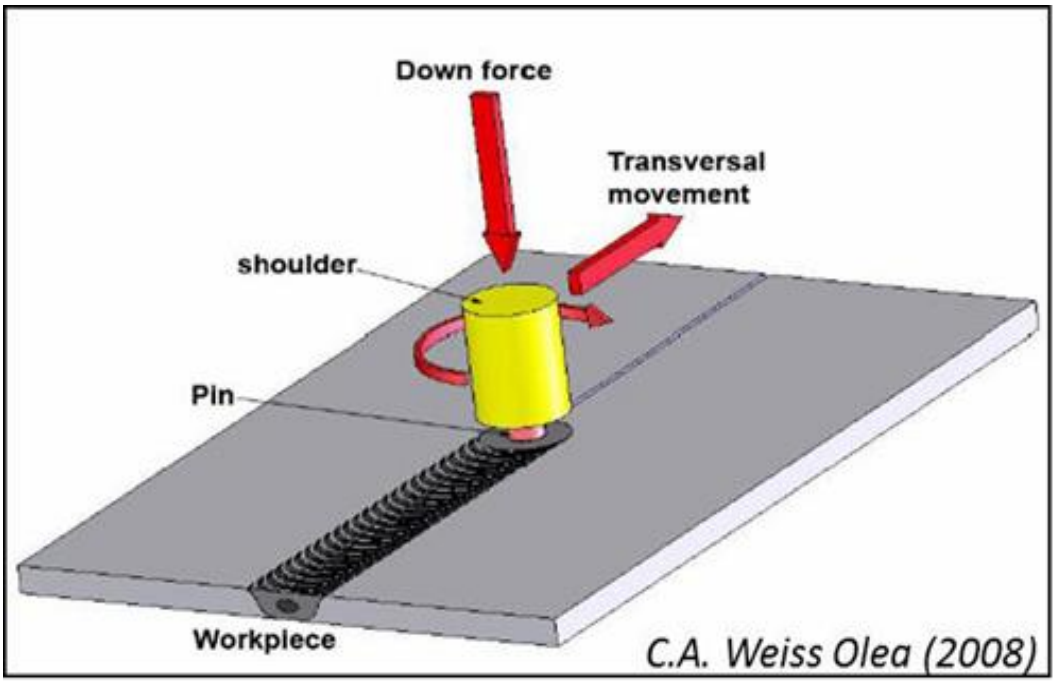

Figure 4.14: Diagram of FSP [88]

4.7.2 Different Parameters Simulated in the Present Study

The present study simulated the tool rotation at six different speeds of 135 rpm, 500 rpm, 1000 rpm, 1500 rpm, 2000 rpm, 2500 rpm as described earlier. Also, six different traverse rates were simulated for linear speeds of 16 mm/min, 25 mm/min, 50 mm/min, 75 mm/min, 100 mm/min, 125 mm/min and the results were presented earlier. The effect of different parameters on the temperature, material flow, and microstructures in SZ and TMAZ zones was evaluated as shown before. Also, the tilt angle of the tool pin was set at 2.5 degrees.

4.7.3 Johnson–Cook Material Model in the Present Study

The present study used the elastic–plastic–hardening isotropic Johnson–Cook material model in all the simulations of AA7075-T6 workpiece under different parametric conditions. Johnson-Cook successfully simulated the plastic deformity of AA7075-T6 in the present study. Johnson–Cook model specifications in the present study are shown in Table 4.4.

Table 4.4: Simulated constants for Johnson-Cook model

Material	A (MPa)	B (MPa)	C	n	m	T Melt (°C)
AA 7075	546	678	0.002	0.14	1.56	630

4.7.4 Taguchi Design of Experiment (DOE) and Optimization

The present study also attempted to optimize the FSP process parameters and used the Taguchi DOE method to ensure the time efficiency of Abaqus®/Explicit simulations as well as find which factor had more significant impact on bonding quality of the weld. The bonding quality of the FSP weld was defined as how symmetrical and well-developed the shape of SZ zone appeared in each Abaqus simulation and any indication about void formation in each Taguchi DOE simulation run. It is important to note that the quality of SZ zone was directly related to the temperature generated by FSP bonding parameters as simulated for each Taguchi run on Abaqus®/Explicit.

The structure of Taguchi method in the present study is presented below. Table 4.5 shows the parameters that were kept constant during FSP simulations based on the results of the present literature search and conclusions reached by some other research studies.

Table 4.5: Tool parameters kept constant

Tool Parameters	Simulation Constant
Pin Tilt Angle	2.5 Degrees
Dwelling Time	2 Seconds
Plunge Depth	4 mm
Plunge Speed	5 mm/second

The FSP process parameters that were varied included rotation speed, transverse speed, and pitch as described before. These process parameters were used as the factors for Taguchi DOE simulations. The six levels for three process parameters were shown earlier in Table 4.3. The present study used fractional factorial Taguchi L_{36} structure with three factors and six levels.

The bonding quality of the FSP joint for each of the above-mentioned simulation experiments was evaluated through Abaqus®/Explicit by checking for symmetrical shape in SZ zone and any formation of voids for each distinct Taguchi simulation run. The effect on plastic strain due to rotation speed and traverse speed simulations helped to gain insights into how symmetric the shape of SZ zone was. Also, Abaqus®/Explicit was used to measure the heat on the surface of the workpiece welds and the results were compared for each Taguchi simulation experiment. The results of simulation experiments showed that the temperatures measured were almost correlated to the pitch ratio (rev/mm) in some portion of the range. The estimations for simulated pitch ratios under various Taguchi simulation experiments were wider than the theoretical limits but were below 30% deviation. The range for pitch ratio simulation estimation was approximately 6-26 rev/min compared to theoretical range of 8.4-20 rev/mm.

The temperatures across the weld were simulated by Abaqus®/Explicit and estimations of the weld tensile strength (TS) were carried out for Experiment Numbers 1-36 in Table 4.6. The goal of Taguchi DOE was to optimize the rotation and traverse speeds and maximize the tensile strength of the weld joint through estimated simulations. Taguchi L_{36} fractional factorial optimization method was used to optimize the study parameters to achieve the highest tensile strength. The structure of Taguchi DOE design with 36 distinct Abaqus®/Explicit simulation runs and estimated tensile strength are shown in Tables 4.6 (a), 4.6 (b), 4.6 (c), 4.6 (d), 4.6 (e), 4.6 (f).

Table 4.6 (a): Taguchi L_{36} fractional factorial DOE 1-6 simulation experiments:

Experiment Number	1	2	3	4	5	6
Levels:						
Rotation Speed (rev/min)	1	1	1	1	1	1
Traverse Speed(mm/min)	1	2	3	4	5	6
Pitch (rev/mm)	1	2	3	4	5	6
Tensile Strength Estimate (MPa)	550	553	555	555	556	559

Table 4.6 (b): Taguchi L_{36} fractional factorial DOE 7-12 simulation experiments:

Experiment Number	7	8	9	10	11	12

Levels:

Rotation Speed (rev/min)	2	2	2	2	2	2
Traverse Speed(mm/min)	1	2	3	4	5	6
Pitch (rev/mm)	2	3	4	5	6	1
Tensile Strength Estimate (MPa)	561	561	566	567	567	569

Table 4.6 (c): Taguchi L_{36} fractional factorial DOE 13-18 simulation experiments:

Experiment Number	13	14	15	16	17	18

Levels:

Rotation Speed (rev/min)	3	3	3	3	3	3
Traverse Speed(mm/min)	1	2	3	4	5	6
Pitch (rev/mm)	3	4	5	6	1	2
Tensile Strength Estimate (MPa)	571	571	574	576	578	580

Table 4.6 (d): Taguchi L_{36} fractional factorial DOE 19-24 simulation experiments:

Experiment Number	19	20	21	22	23	24

Levels:

Rotation Speed (rev/min)	4	4	4	4	4	4
Traverse Speed(mm/min)	1	2	3	4	5	6
Pitch (rev/mm)	4	5	6	1	2	3
Tensile Strength Estimate (MPa)	571	565	560	558	550	549

Table 4.6 (e): Taguchi L_{36} fractional factorial DOE 25-30 simulation experiments:

Experiment Number	25	26	27	28	29	30

Levels:

Rotation Speed (rev/min)	5	5	5	5	5	5
Traverse Speed (mm/min)	1	2	3	4	5	6
Pitch (rev/mm)	5	6	1	2	3	4
Tensile Strength Estimate (MPa)	542	536	532	526	519	510

Table 4.6 (f): Taguchi L_{36} fractional factorial DOE 31-36 simulation experiments:

Experiment Number	31	32	33	34	35	36

Levels:

Rotation Speed (rev/min)	6	6	6	6	6	6
Traverse Speed (mm/min)	1	2	3	4	5	6
Pitch (rev/mm)	6	1	2	3	4	5
Tensile Strength Estimate (MPa)	502	493	484	475	467	458

Based on Taguchi DOE experiment, the optimum value for estimated tensile strength was determined. In the present study, increasing the rotational speed from 135 rpm to 1500 rpm generated increased tensile strength in FSP weld joint. Therefore, 1500 rpm was the best choice under the tool and parameter simulations in the present study. Also, the simulation results showed that the FSP welds at lower pitch ratios generated better bonding between the two AA7075-T6 plates. The increase in traverse speed up to 50 mm/min helped to increase the tensile strength but further traverse speeds resulted in weaker tensile strengths. Therefore, 50 mm/min was the best option for travers speed. The combination of 1500 rpm rotation, 50 mm/min traverse, and 20 rev/mm pitch was found to be the most optimum FSP process parameters to generate the highest tensile strength (TS) at 580 (MPa). The corresponding estimated yield strength (YS) was 450 (MPa). The present study increased the rotation speed and traverse speed while keeping the pitch constant for majority of Taguchi experiments. However, the estimation results showed weaker joints at very high rotational and traverse speeds.

The higher the tool speed, the lower the tensile strength as shown in Tables 4.6 (d), 4.6(e), 4.6 (f).

In line with several previous studies, the present study used an unthreaded cylindrical tool pin to simulate the material flow in SZ and TMAZ zones. It was shown by a previous study that SZ material flow caused by an unthreaded cylindrical tool pin has the same features as a threaded tool [94]. In addition, the simulated Taguchi optimization results in the present study were generally in agreement with previous experimental studies related to FSP/FSW of AA7075-T6 similar and dissimilar weld joints [95, 96, 97, 98, 99, 100, 101, 102, 103, 104, 105].

4.7.5 Validation of the Results in the Present Study

The findings from the present Abaqus® 3-D finite element model (FEM) model were validated. For validation, the results of the present FSP processing study were compared with the findings reported by other researchers who also studied AA7075-T6 workpiece under various FSP/FSW processing parameters. In agreement with majority of other published studies, the present study used Abaqus®/Explicit to investigate the thermo-mechanical behaviors of AA7075-T6 alloy under different FSP processing parameters. In addition, several other published FEM studies had validated their simulation findings with additional experimental study with physical processing of the workpiece. AA7075-T6 thermo-mechanical simulation results achieved by the present study are in general agreement with simulations and experimental findings in previous studies despite some differences in workpiece size, processing parameters, tool pin size and shape [66, 67, 74, 89-105].

The results of the present study were validated with above-mentioned twenty studies. The validation results of five selected studies [67, 74, 91, 97, 104] are presented below.

The results of the present study demonstrated that higher material transfer occurred with increasing tool pin rotational speeds. Similarly, another study found bigger material transfer at higher rotation speeds. The result of that validation study is shown in Figure 4.15 [67].

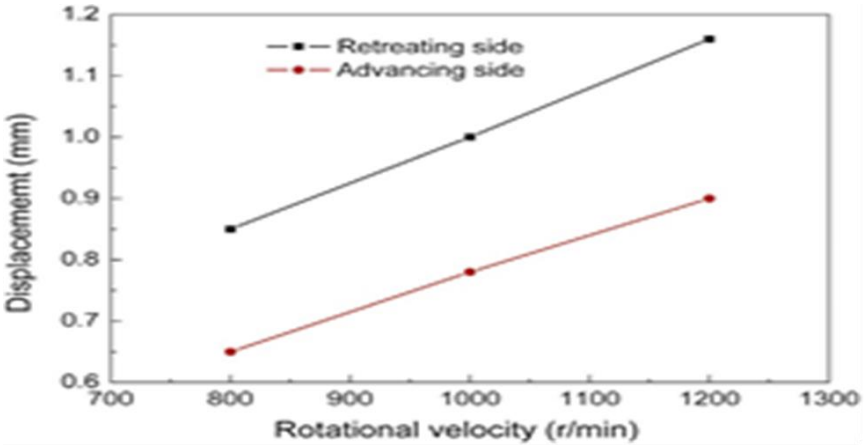

Figure 4.15: Higher material transfer at higher rotation [67]

As mentioned earlier, the peak temperature in the present FSP study was 440 °C. In addition, the temperature in the present study decreased with more distance from the FSP joint center line as described earlier. Another study (Zhu et al., 2017) reported similar results with peak temperature of 450 °C and decreasing temperature with increasing distance from the joint path centerline as shown in Figure 4.16 [74].

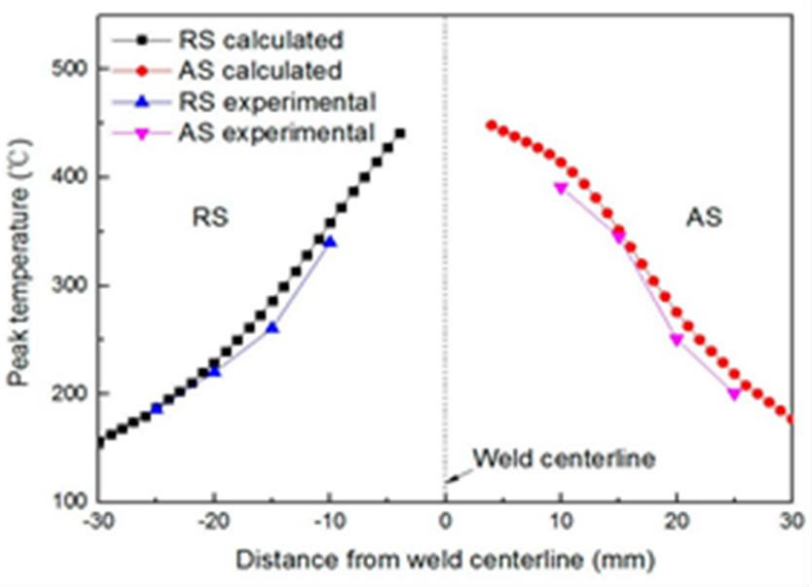

Figure 4.16: Peak temperature decrease from joint path [74]

The present study achieved optimum tensile strength result with 1500 rpm rotation speed and 50 mm/min linear traverse speed as determined by Taguchi Design of Experiment (DOE) optimization. Another study (Rajakumar et al., 2010) similarly found optimum results for tensile strength with 1400 rpm rotation speed and 60 mm/min linear traverse speed as shown in Figure 4.17 [91].

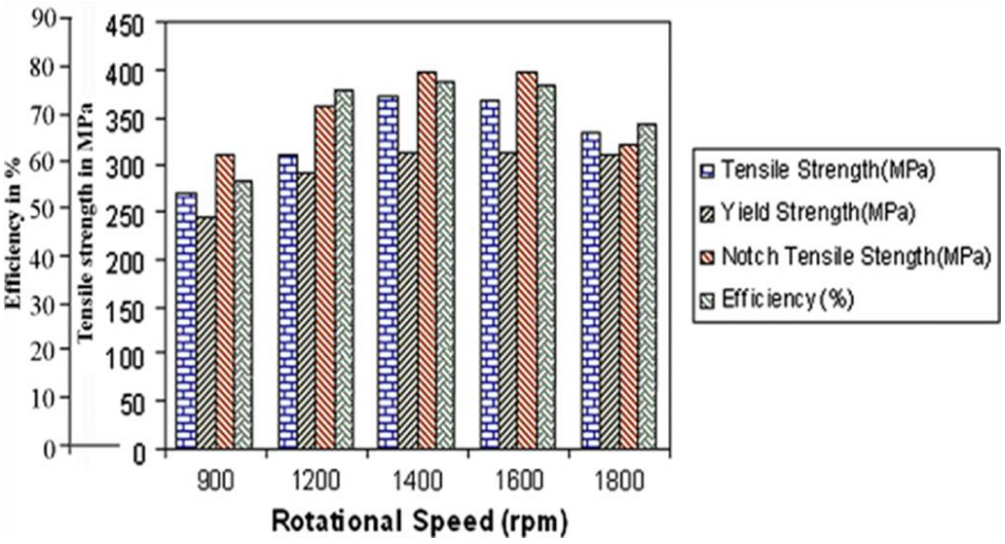

Figure 4.17: Optimum tensile strength at 1400 rpm and 60 mm/min [91]

As shown earlier in Table 4.1, the optimization result of the present study showed that optimum tensile strength was obtained at a rotational speed of 1500 rpm. Additionally, the present study showed that both tensile strength and yield strength decreased above 1500 rpm rotation speed. Another study (Roshan et al., 2013) found similar results at tensile strength of 1400 rpm. Also, this validation study found that both tensile strength and yield strength decreased above 1400 rpm rotation speed as demonstrated in Figure 4.18 (a) (b) [97].

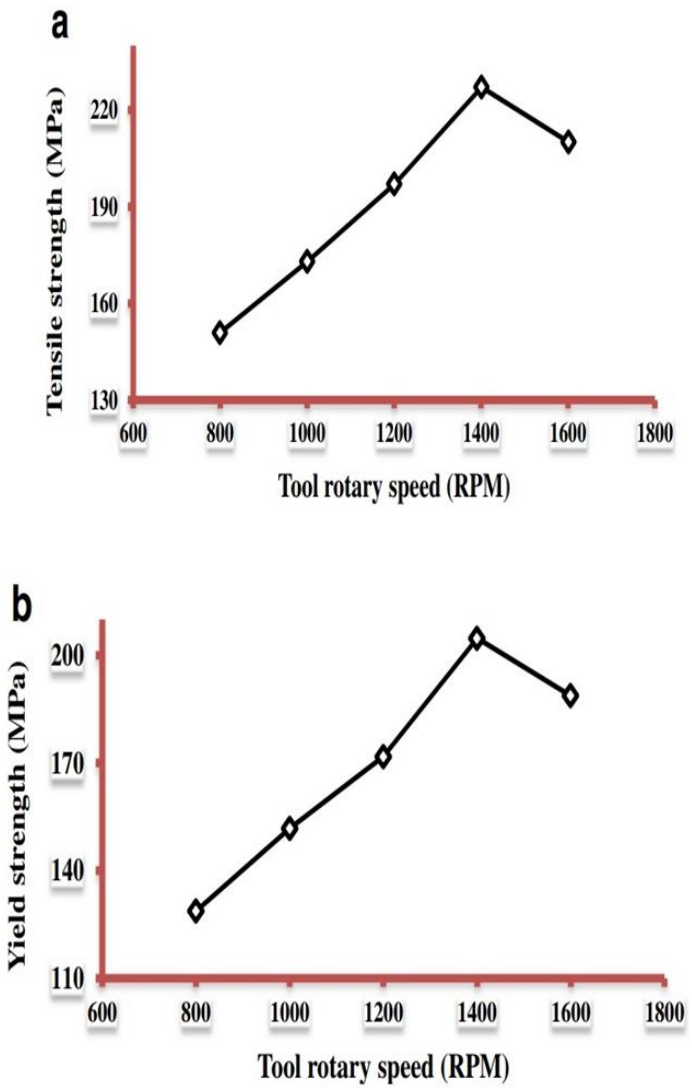

Figure 4.18: Optimum tensile strength (a) and yield strength (b) [97]

As indicated before, the present study concluded that 1500 rpm rotation speed and 50 mm/min traverse speed generated the optimized tensile strength. Another study (Kumar et al., 2020) achieved optimum tensile strength at 1120 rpm rotation speed and 40 mm/min traverse speed. The results of both studies were similar. Figure 4.19 shows the results of tensile strength associated with tool optimum rotation speed of 1120 rpm (top figure) and optimum traverse feed of 40 mm/min (bottom figure) [104].

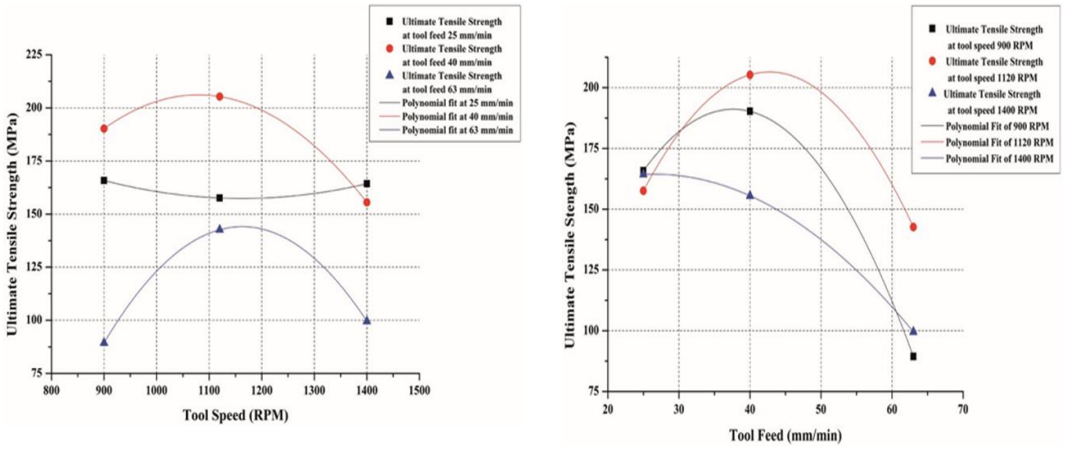

Figure 4.19: Optimum rotation 1120 rpm and traverse 40 mm/min [104].

Chapter 5

CONCLUSION

The current study used Abaqus®/Explicit software and developed 3D simulation models for FSP processing in joining two identical AA7075-T6 plates under six different rotation speeds and six different linear traverse speeds. The tool was modeled using Lagrangian model and the workpiece was modeled with Eulerian technique. The model simulated the plunging, dwelling, and traverse stages in FSP processing. The study showed a significant rise in workpiece temperature below the pin contact surface when the tool started to penetrate into AA 7075-T6 workpieces. Peak FSP temperatures were generated which were below AA 7075–T6 melting point. The simulations demonstrated that the material located close to surface moved toward the bottom and the middle material moved toward the top surface. The model for TMAZ zone demonstrated that FSP advancing side experienced a smaller material displacement compared to the retreating side. The displacement of material located close to bottom of TMAZ zone was almost zero. An interesting finding from the simulation results proved that the highest material transfer occurred during the final FSP stage.

The simulations in the present study demonstrated that complex trade-off analysis is required to properly select and balance many parameters to create a successful FSP bonding joint. It is important to carefully review the tool size, shape, material hardness, and tilt angle. Also, the selection of workpiece materials and the dimensions of the

workpiece must be assessed. In addition, it is critical to select the right combination of parameters for FSP processing especially for rotational and linear traverse velocities. This analysis is needed to perform a successful bonding of workpiece materials. The present study deployed Taguchi DOE optimization and determined the optimum process parameters were 1500 rpm rotation, 50 mm/min traverse, and 20 rev/mm pitch to achieve the highest tensile strength.

This study has achieved all its objectives for analyzing the thermo-mechanical behaviors of AA7075-T6 under different FSP processing conditions. The simulation results for AA7075-T6 alloy as well as Taguchi DOE optimization as modeled in the present study were in general agreement with the published findings reported in several other experimental and simulation studies conducted by other researchers around the world.

The results and validation achieved by the present study have demonstrated that Abaqus®/Explicit is a powerful tool for developing optimized and realistic 3D numerical models for FSP processing.

REFERENCES

[1] Geller, T. Aluminum: Common Metal, Uncommon Past. (2007, December 2). Retrieved from https://www.sciencehistory.org/distillations/aluminum-common-metal-uncommon-past

[2] Donoghue, A.M., Frisch, N., & Olney, D. (2014). Bauxite Mining and Alumina Refining. *Journal of Occupational and Environmental Medicine, 56, Number 5S*, S12-S17.

[3] Jonsson, C. (2018). How to choose the right aluminum alloy. Retrieved from https://www.shapesbyhydro.com/en/material_properties/how-to-choose-the-right-aluminium-alloy/ToPdf?printview=true

[4] Gandara, M.J.F. (2013). Aluminium: The Metal of Choice. *Materials and Technology, 47*, 261-265.

[5] Automotive Aluminum market size, share & trends analysis report by end use (passenger cars, light commercial vehicles, heavy commercial vehicles), by application, and segment forecasts, 2019 – 2025. (2019, July). Retrieved from https://www.grandviewresearch.com/industry-analysis/automotive-aluminum-market#:~:text=Industry%20Insights,are%20the%20key%20growth%20drivers.

[6] Automotive Aluminum in cars and trucks. The Aluminum association. (2020, November 26). Retrieved from https://www.aluminum.org/product-markets/automotive

[7] High strength Aluminum alloys market size, share & trends analysis report by application (aerospace, automotive, railway & marine, defense & space), by region, and segment forecasts, 2020 – 2027. (2020, May). Retrieved from https://www.grandviewresearch.com/industry-analysis/high-strength-aluminum-alloys-market

[8] Pankade, S.B., Khedekar, D.S., & Gogte, C.L. (2018). The influence of heat treatments on electrical conductivity and corrosion performance of AA7075-T6 Aluminum alloy. *Procedia Manufacturing, 20,* 53-58.

[9] Alcoa 7075 data sheet (PDF). Understanding cold finished Aluminum alloys (2004, May). Retrieved from https://www.spacematdb.com/spacemat/manudatasheets/alcoa_alloy_7075.pdf

[10] Understanding the alloys of aluminum (2020, November 25). Retrieved from http://www.alcotec.com/us/en/education/knowledge/techknowledge/understanding-the-alloys-of-aluminum.cfm#

[11] Kumar, P.V., Reddy, G.M., & Rao, K.S. (2015). Microstructure, mechanical and corrosion behavior of high strength AA7075 aluminum alloy friction stir welds - Effect of post weld heat treatment. *Defence Technology, 11*, 362-369.

[12] Aghdam, N.J., Hassanifard, N., Ettefagh, M, & Nanvayesavojblaghi, A. (2014). Investigating fatigue life effects on the vibration properties in friction stir spot welding using experimental and finite element modal analysis. *Strojniski vestnik -Journal of Mechanical Engineering, 60*, 735-741.

[13] Young, P. The Complete History of Welding (2020, November 11). Retrieved from https://weldingheadquarters.com/history-of-welding/

[14] Lee, J.H., Park, S.H., Kwon, H.S., Kim G.S., & Lee C.S. (2014). Laser, tungsten inert gas, and metal active gas welding of DP780 steel: comparison of hardness, tensile properties and fatigue resistance. *Materials & Design, 64*, 559-565.

[15] Akca, E. & Gursel, A. (2016). Solid state welding and application in aeronautical industry. *Periodicals of Engineering and Natural Sciences (PEN), 4*, 1-8.

[16] Friction stir welding – enabling worldwide engineering success (2012, November 1). Retrieved from https://news.cision.com/twi-ltd/r/friction-stir-welding---enabling-worldwide-engineering-success,c9329661

[17] Thomas, W.M., Johnson, K.I., & Wiesner, C.S. (2003). Friction Stir Welding – Recent Developments in Tool and Process Technologies. *Advanced Engineering Materials, 5*, 485-490

[18] Rao M. S., Prakash K. J., & Kumar B. V. R. (2013). A review of friction stir welding process and its variables. *International Journal of science and Research (IJSR), 2*, 375-379

[19] Threadgill, P. L., Leonard, A. J., Shercliff, H. R., & Withers P. J. (2009). Friction stir welding of aluminum alloys. *International Materials Reviews, 54*, 49-93

[20] Prasanna, P., Penchalayya, C., & Rao, D.A. (2013). Effect of tool pin profiles and heat treatment process in the friction stir welding of AA 6061. *American Journal of Engineering Research (AJER), 2*, 7-15

[21] Mishra, R.S., & Ma, Z.Y. (2005). Friction stir welding and processing. *Materials Science and Engineering, 50*, 1-78

[22] Mishra, R.S., Mahoney, M.W., McFadden, S.X., Mara, N.A., & Mukherjee, A.K. (1999). High strain rate superplasticity in a friction stir processed 7075 Al alloy. *Scr. Mater., 42*, 163–168.

[23] Li, K., Liu, X., & Zhao, Y. (2019). Research Status and Prospect of Friction Stir Processing Technology. *Coatings, 9*, 129-139.

[24] Zhang, Y. N., Cao, X., Larose, S., & Wanjara, P. (2012). Review of tools for friction stir welding and processing. *The Canadian Journal of Metallurgy and Materials Science, 51*, 250-261.

[25] Ma, Z. Y., Feng, A. H., Chen, D. L., & Shen, J. (2018). Recent Advances in Friction Stir Welding/Processing of Aluminum Alloys: Microstructural Evolution and Mechanical Properties. *Critical Reviews in Solid State and Materials Sciences, 43*, 269-333.

[26] Patel, V., Li, W., Vairis, A., & Badheka, V. (2019). Recent Development in Friction Stir Processing as a Solid-State Grain Refinement Technique:

Microstructural Evolution and Property Enhancement. *Critical Reviews in Solid State and Materials Sciences, 44*, 378-426.

[27] Ma, Z.Y. (2008). Friction stir processing technology: A review. *Metallurgical and Materials Transactions A, 39*, 642–658.

[28] Aghdam, N.J., Hassanifard, S., Ettefagh, M.M., & Nanvayesavojblaghi, A. (2014). Investigating Fatigue Life Effects on the Vibration Properties in Friction Stir Spot Welding Using Experimental and Finite Element Modal Analysis. *Strojniikivestnik Journal of Mechanical Engineering 60*, 735-741.

[29] Jana, S., Mishra, R.S., Baumann, J.B., & Grant, G. (2010). Effect of friction stir processing on fatigue behavior of an investment cast Al-7Si-0.6 Mg alloy. Acta Materialia, 58, 989-1003.

[30] Padhy, G.K., Wu, C.S., & Gao, S. (2017). Friction stir based welding and processing technologies—Processes, parameters, microstructures and applications: A review. *Journal of Materials Science & Technology, 34*, 1–38.

[31] Tamadon, A., Pons, D.J., Sued, K., & Clucas, D. (2017). Development of metallographic etchants for the microstructure evolution of A6082-T6 BFSW welds. *Metals, 7*, 423-440.

[32] Xin, R.L., Zheng, X., Liu, Z., Liu, D., Qiu, R.S., Li, Z.Y., & Liu, Q. (2016). Microstructure and texture evolution of an Mg-Gd-Y-Nd-Zr alloy during friction stir processing. *Journal of Alloys and Compounds, 659*, 51–59.

[33] Wang, L.Q., Xie, L.C., Lv, Y.T., Zhang, L.C., Chen, L.Y., Meng, Q., Qu, J., Zhang, D., & Lu, W.J. (2017). Microstructure evolution and superelastic behavior in Ti-35Nb-2Ta-3Zr alloy processed by friction stir processing. *Acta Materialia, 131*, 499–510.

[34] Wang, Y.B., Huang, Y.X., Meng, X.C., Wan, L., & Feng, J.C. (2017). Microstructural evolution and mechanical properties of Mg-Zn-Y-Zr alloy during friction stir processing. *Journal of Alloys and Compounds*, *696*, 875–883.

[35] Tamadon, A., Pons, D.J., Sued, K., & Clucas, D. (2018). Thermomechanical grain refinement in AA6082-T6 thin plates under bobbin friction stir welding. *Metals, 8*, 375-395.

[36] Yang, Q., Xiao, B.L., Ma, Z.Y., & Chen, R.S. (2011). Achieving high strain rate superplasticity in Mg-Zn-Y-Zr alloy produced by friction stir processing. *Scripta Materialia, 65*, 335–338.

[37] Oh-Ishi, K. & McNelley, T.R. (2005). The influence of friction stir processing parameters on microstructure of as-cast NiAl bronze. Metallurgical and Materials Transactions A, 36, 1575–1585.

[38] Ma, Z. Y., & Mishra, R. S. (2005). Development of ultrafine-grained microstructure and low temperature (0.48 Tm) superplasticity in friction stir processed Al-Mg-Zr. *Scripta Materialia, 53*, 75-80.

[39] Sathiskumar, R., Murugan, N., Dinaharan, I., & Vijay, S.J. (2013). Role of friction stir processing parameters on microstructure and microhardness of boron carbide particulate reinforced copper surface composites. *Sadhana Academy Proceedings in Engineering Sciences, 38,* 1433–1450.

[40] Khodabakhshi, F., Gerlich, A.P., & Svec, P. (2017). Fabrication of a high strength ultra-fine-grained Al-Mg-SiC nanocomposite by multi-step friction-stir processing. *Materials Science & Engineering A: Structural Materials: Properties, Microstructure and Processing, 698,* 313–325.

[41] Morishige, T., Tsujikawa, M., Hino, M., Hirata, T., Oki, S., & Higashi, K. (2008). Microstructural modification of cast Mg alloys by friction stir processing. *International Journal of Cast Metals Research, 21*, 109–113.

[42] Morishige, T., Hirata, T., Tsujikawa, M., Higashi, K. (2010). Comprehensive analysis of minimum grain size in pure aluminum using friction stir processing. *Materials Letters, 64*, 1905-1908.

[43] Hannard, F., Castin, S., Maire, E., Mokso, R., Pardoen, T., & Simar, A. (2017). Ductilization of aluminium alloy 6056 by friction stir processing. *Acta Materialia, 130,* 121-136.

[44] El-Rayes, M., & El-Danaf, EA. (2012). The influence of multi-pass friction stir processing on the microstructural and mechanical properties of Aluminum Alloy 6082. *Journal of Materials Processing Technology, 212*, 1157–1168.

[45] Costa, M.I., Verdera, D., Vieira, M.T., & Rodrigues, D.M. (2014). Surface enhancement of cold work tool steels by friction stir processing with a pinless tool. *Applied Surface Science, 296*, 214–220.

[46] Hosseini, S.A., Ranjbar, K., Dehmolaei R., & Amirani, A.R. (2015). Fabrication of Al5083 surface composites reinforced by CNTs and cerium oxide nano particles via friction stir processing. *Journal of Alloys and Compounds, 622*, 725-733.

[47] Garcia-Bernal, M.A., Mishra, R.S., Verma, R., & Hernandez-Silva, D. (2016). Influence of friction stir processing tool design on microstructure and superplastic behavior of Al-Mg alloys. Mater. Sci. Eng. A Struct. Mater. Prop. Microstruct. Process. 2016, 670, 9–16.

[48] Patel, V.V., Badheka, V.J., & Kumar, A. (2016). Influence of Pin Profile on the Tool Plunge Stage in Friction Stir Processing of Al–Zn–Mg–Cu Alloy. *Transactions of The Indian Institute of Metals, 70*, 1151–1158.

[49] Mahmoud, E.R.I., Takahashi, M., Shibayanagi, T., & Ikeuchi, K. (2009). Effect of friction stir processing tool probe on fabrication of SiC particle reinforced composite on aluminum surface. Science and Technology of Welding and Joining, 14, 413–425.

[50] Mishra, R.S., Ma, Z.Y., & Charit, I. (2003). Friction stir processing: A novel technique for fabrication of surface composite. *Materials Science and*

Engineering: A Structural Materials: Properties, Microstructure and Processing, 341, 307–310.

[51] Tonelli, L., Morri, A., Toschi, S., Shaaban, M., Ammar, H., Ahmed, M.M.Z., Ramadan, R., El-Mahallawi, I., & Ceschini, L. (2019). Effect of FSP parameters and tool geometry on microstructure, hardness, and wear properties of AA7075 with and without reinforcing B4C ceramic particles. The International Journal of Advanced Manufacturing Technology, 102, 3945–3961.

[52] Ji, Y.S., Hidetoshi, F., Nakata, K, Kimura, H., Inoue, A., & Nogi, K. (2008). Friction stir welding of Zr55Cu30Ni5Al10 bulk metallic glass. Journal of Physics: Conference Series, 165, 1-4.

[53] Ni, D.R., Wang, J.J., Zhou, Z.N., & Ma, Z.Y. (2014). Fabrication and mechanical properties of bulk NiTip/Al composites prepared by friction stir processing. *Journal of Alloys and Compounds, 586*, 368–374.

[54] Arab, S.M., Karimi, S., Jahromi, S.A.J., Javadpour, S., Zebarjad, S.M. (2015). Fabrication of novel fiber reinforced aluminum composites by friction stir processing. *Materials Science & Engineering A, 632*, 50–57.

[55] Ghasemi-Kahrizsangi, A., & Kashani-Bozorg, S.F. (2012). Microstructure and mechanical properties of steel/TiC nano-composite surface layer produced by friction stir processing. *Surface and Coatings Technology, 209*, 15–22.

[56] Asadi, P., Faraji,,G., Masoumi, A., & Givi, M.K.B. (2011). Experimental investigation of magnesium-base nanocomposite produced by friction stir processing: effects of particle types and number of friction stir processing passes. *Metallurgical and Materials Transactions A, 42*, 2820–2832.

[57] Huang, Y., Wang, T., Guo, W., Wan, L., & Lv, S. (2014). Microstructure and surface mechanical property of AZ31 Mg/SiCp surface composite fabricated by direct friction stir processing. *Materials and Design, 59*, 274–278.

[58] Khodabakhshi, F., Haghshenas, M., Chen, J., Shalchi-Amirkhiz, B., Li, J., & Gerlich, A.P. (2017). Bonding mechanism and interface characterisation during dissimilar friction stir welding of an aluminium/polymer bi-material joint. *Science and Technology of Welding and Joining, 22*, 182–190.

[59] Avettand-Fènoël, M.N., Simar, A., Shabadi, R., Taillard, R., & Meester, B. (2014). Characterization of oxide dispersion strengthened copper based materials developed by friction stir processing. *Materials and Design, 60*, 343–357.

[60] Orozco-Caballero, A., Ruano, O.A., Rauch, E.F., & Carreno, F. (2018). Severe friction stir processing of an Al-Zn-Mg-Cu alloy: Misorientation and its influence on superplasticity. *Materials & Design, 137*, 128–139.

[61] Carreño, F., & Orozco-Caballero, A. (2018). Superplastic GBS Constitutive equation incorporating average grain misorientation dependence. *Materials Science Forum, 941*, 1501–1506.

[62] Maamoun, A.H., Veldhuis, S.C., & Elbestawi, M. (2019). Friction stir processing of AlSi10Mg parts produced by selective laser. *Journal of Materials Processing Technology, 263*, 308-320.

[63] Mukherjee, S., & Ghosh, A. K. (2011). Friction stir processing of direct metal deposited copper–nickel 70/30. *Materials Science and Engineering A, 528*, 3289-3294.

[64] Santos, T.G., Lopes, N., Machado, M., Vilaça, P., & Miranda, R.M. (2015). Surface reinforcement of AA5083-H111 by friction stir processing assisted by electrical current. *Journal of Materials Processing Technology, 216*, 375-380.

[65] Bauri, R., Yadav, D., & Suhas, G. (2011). Effect of friction stir processing (FSP) on microstructure and properties of Al–TiC in situ composite. *Materials Science and Engineering A, 528*, 4732–4739.

[66] Salloomi, K.N., Hussein, F.I., & Al-Sumaidae, S.N.M. (2020). Temperature and Stress Evaluation during Three Different Phases of Friction Stir Welding of AA 7075-T651 Alloy. *Modelling and Simulation in Engineering, 2020*, 1-11.

[67] Ji, S.D., Jin, Y.Y., Yue, Y.M., Gao, S.S., Huang, Y.X., & Wang, L. (2013). Effect of temperature on materials transfer behavior at different stages of friction stir welded 7075-T6 Aluminum alloy. *Journal of Materials Science & Technology, 29*, 955-960.

[68] Ahadi, A., & Port, F.R. (2019). Fully coupled thermo-mechanical modelling of the initial phase of the friction stir welding process using finite element analysis. *Advances in Metallurgical and Material Engineering, 2*, 39-60.

[69] Aziz, S.B., Dewan1, M.W., Huggett, D.J., Wahab, M.A., Okeil, A.M., & Liao, T.W. (2018). A fully coupled thermomechanical model of friction stir welding (FSW) and numerical studies on process parameters of lightweight Aluminum alloy joints. *Acta Metallurgica Sinica (English Letters)[J], 31*,1-18.

[70] Fashami, H.A.A., Gollo, M.H., Arab, N.B.M., & Nami, B. (2019). The numerical modeling to study the multi-pass friction stir processing on Magnesium casting alloy AZ91. *International Journal of Advanced Design and Manufacturing Technology, 12*, 9-16.

[71] Ansari, M.A., Samanta, A., Behnagh, R.A., & Ding, H. (2019). An efficient coupled Lagrangian-Eulerian finite element model for friction stir processing. *The International Journal of Advanced Manufacturing Technology, 101*, 1495-1508.

[72] Iordache, M., Badulescu, C., Iacomi, D., Nitu, E. & Ciuca, C. (2016). Numerical simulation of the friction stir welding process using coupled Eulerian Lagrangian method. *Materials Science and Engineering, 145*, 1-7.

[73] Kishta, E.E.M., Abed, F.H., & Darras, B.M. (2014). Nonlinear finite element simulation of friction stir processing of marine grade 5083 Aluminum alloy. *Engineering Transactions, 62*, 313-328.

[74] Zhu, Z., Wang, M., Zhang, H., Zhang, X., Yu, T., and Wu,, Z. (2017). A finite element model to simulate defect formation during friction stir welding. *Metals, 7*, 1-15.

[75] Meyghani, B., Awang, M. & Wu, C.S. (2020). Finite element modeling of friction stir welding (FSW) on a complex curved plate. *Journal of Advanced Joining Processes 1,* 1-11.

[76] ASM Material Data Sheet AA7075-T6. (2020, November 15). Retrieved from http://asm.matweb.com/search/SpecificMaterial.asp?bassnum=MA7075T6

[77] Starting Abaqus/CAE. (2020, December 2). Retrieved from https://abaqus-docs.mit.edu/2017/English/SIMACAEGSARefMap/simagsa-c-bsstartcae.htm

[78] Overview of Eulerian analyses. (2020, December 5). Retrieved from https://abaqus-docs.mit.edu/2017/English/SIMACAECAERefMap/simacae-t-adveulerianoverview.htm

[79] Benson, D.J., & Okazawa, S. (2004). Contact in a multi-material Eulerian finite element formulation. *Computer methods in applied mechanics and engineering, 193,* 4277-4298.

[80] Eulerian analysis. (2020, November 11). Retrieved from https://abaqus-docs.mit.edu/2017/English/SIMACAEANLRefMap/simaanl-c-eulerianananalysis.htm

[81] About surfaces. Why use surfaces? (2020, November 12). Retrieved from https://abaqus-ocs.mit.edu/2017/English/SIMACAEMODRefMap/simamod-c-surfoverview.htm

[82] Eulerian surface definition. (2020, November 13). Retrieved from https://abaqus-ocs.mit.edu/2017/English/SIMACAEMODRefMap/simamod-c-eulsurf.htm

[83] Eulerian elements. (2020, November 14). Retrieved from https://abaqus-docs.mit.edu/2017/English/SIMACAEELMRefMap/simaelm-c-eulerianelem.htm

[84] Eulerian element library. (2020, November 15). Retrieved from https://abaqus-docs.mit.edu/2017/English/SIMACAEELMRefMap/simaelm-r-eulerianelemlib.htm

[85] Thermal loads. (2020, November 16). Retrieved from https://abaqus-docs.mit.edu/2017/English/SIMACAEPRCRefMap/simaprc-c-thermal.htm

[86] User subroutine VDFLUX. (2020, November 16). Retrieved fromhttps://abaqus-docs.mit.edu/2017/English/SIMACAESUBRefMap/simasub-c-vdflux.htm

[87] Mishra, R. S., & Mahoney, M.W. (2007). Friction Stir Welding and Processing. ASM International, ISBN: 978-0-87170-840-3, 1-368.

[88] Olea, C. A. W. (2008). Influence of Energy Input in Friction Stir Welding on Structure Evolution and Mechanical Behavior of Precipitation-Hardening in

Aluminium Alloys (AA2024-T351, AA6013-T6 and Al-Mg-Sc). GKSS Forschungszentrum Geesthacht, GmbH, Geesthacht. 1-149.

[89] Buffa, G., Fratini, L. & Pasta, S. (2009). Residual stresses in friction stir welding: Numerical Simulation and experimental verification. *International Centre for Diffraction Data, ISSN 1097-0002*, 444-453.

[90] Zhang, J., Upadhyay, P., Hovanski, Y., & Field, D.P. (2017). High-Speed Friction Stir Welding of AA775-T6 Sheet: Microstructure, Mechanical Properties, Micro-Texture, and Thermal History. Metallurgical and Materials Transactions A, 49, 210-222.

[91] Rajakumar, S., Muralidharan, C., & Balasubramanian, V. (2010). Influence of friction stir welding process and tool parameters on strength properties of AA7075-T6 Aluminum alloy joints. *Materials and Design, 32*, 535-549.

[92] Rajakumar, S., Muralidharan, C., & Balasubramanian, V. (2009). Optimization of the friction-stir-welding process and tool parameters to attain a maximum tensile strength of AA7075-T6 Aluminum alloy. *Proceedings of the Institution of Mechanical Engineers Part B Journal of Engineering Manufacture, 224*, 1175-1191.

[93] Shah, P.H., & Badheka, V. (2016). An Experimental Investigation of Temperature Distribution and Joint Properties of Al 7075 T651 Friction Stir Welded Aluminium Alloy. Procedia Technology, 23, 543-550.

[94] Lorrain, O., Favier, V., Zahrouni, H., & Lawrjaniec, D. (2010). Understanding the material flow path of friction stir welding process using unthreaded tools. *Journal of Materials Processing Technology, Elsevier, 210*, 603-609.

[95] Selvarajan, R., & Balasubramanian, V. (2012). Predicting grain size and tensile strength of friction stir welded joints of AA7075-T6 Aluminum alloy. *Materials and manufacturing processes, 27:1*, 78-83.

[96] Naik, L.S., Hadya, B., & Murahari, K. (2018). Experimental study on AA7075 its effect of rotational speed and tool pin profile on friction stir welding process. *International Journal of Innovations in Engineering and Technology*, *9*, 88-93.

[97] Roshan, S.B., Jooibari, M.B., Teimouri, R., Asgharzadeh-Ahmadi, G., Falahati-Naghibi, M., & Sohrabpoor, H. (2013). Optimization of friction stir welding process of AA7075 aluminum alloy to achieve desirable mechanical properties using ANFIS models and simulated annealing algorithm. *The International Journal of Advanced Manufacturing Technology, Springer*, 1-17.

[98] Butola, R., Ranganath, M.S., & Murtaza, Q. (2019). Fabrication and optimization of AA7075 matrix surface composites using Taguchi technique via friction stir processing (FSP). *Engineering Research Express 1*, 1-11.

[99] Abd Elnabi, M.M., Elshalakany, A.B., Abdel-Mottaleb, M.M., Osman, T.A., & El Mokadem, A. (2019). Influence of friction stir welding parameters on metallurgical and mechanical properties of dissimilar AA5454-AA7075

Aluminum alloys. *Journal of Materials Research and Technology,8(2),* 1684-1693.

[100] Padmanaban, R., Balusamy, V., Saikrishna, V, & Niranthar, K.G. (2014). Simulated annealing based parameter optimization for friction stir welding of dissimilar Aluminum alloys. *Procedia Engineering, 97,* 864-870.

[101] Bayazid, S.M., Farhangi, H., & Ghahramani, A. (2015). Investigation of friction stir welding parameters of 6063-7075 Aluminum alloys by Taguchi method. *Procedia Materials Science 11*, 6-11.

[102] Reddy, A.G., Saketh, Ch., Padmanaban, R., & Balusamy, V. (2013). Process parameter optimization for friction stir welding of dissimilar Aluminum alloys. *International Journal of Engineering Research & Technology, 2:10,* 3281-3288.

[103] Maleki, E. (2015). Artificial neural networks application for modeling of friction stir welding effects on mechanical properties of 7075-T6 Aluminum alloy. *4th Global Conference on Materials Science and Engineering, 103*, 1-15.

[104] Kumar, G., Kumar, R., & Kumar, R. (2020). Optimization of process parameters of friction stir welded AA5082-AA7075 butt joints using resonance fatigue properties. *Bulletin of the Polish Academy of Sciences Technical Sciences, 68 (1),* 99-108.

[105] Laska, A., & Szkodo, M. (2020). Manufacturing parameters, materials, and welds properties of butt friction stir welded joints-overview. *Materials, 13*, 1-46.